

Response to Review report for “OMI Total Column Water Vapour Version 4: Validation and Applications”

by Huiqun Wang, Amir Hossein Souri, Gonzalo Gonzalez Abad, Xiong Liu, and Kelly Chance

General comments

In this manuscript, the version 4 TCWV retrieval from OMI is validated against ground-based GPS TCWV retrievals over land and SSMIS satellite microwave retrievals over land. Differences of the version 4 retrieval with previous versions have been described, although a detailed analysis of the improvement with respect to the previous version is still lacking. I will point out some specific examples where such an additional comparison might be included in the manuscript. Also the interpretation of some of the findings for the OMI TCWV differences with TCWV from GPS or SSMIS is lacking, see again below in my specific comments. Thereafter, 3 well-chosen examples show the importance of having a global TCWV dataset, here from OMI. These are nice demonstrations of the TCWV product, but the authors might argue more what the added value of in particular OMI TCWV (and version 4) is for those applications, compared to other satellite retrievals or reanalyses.

Thank you very much for the thorough and constructive review. We have improved the manuscript following your suggestions. The example applications are intended to test and show that there is value in the OMI TCWV dataset, and therefore, the data can contribute to the overall understanding of water vapor. Comparisons with other satellite datasets or reanalyses for the added value of OMI TCWV are left for future work.

Please find our detailed response below.

Specific comments

□ Page 1, line 10: I would write out “OMI” already in the abstract, as well as WRF (on line 28).

We have now written them out.

□ Page 2-3, lines 58 –60: to me, it is strange to already mention a result of the analysis in the introduction of the manuscript. I would drop this sentence.

The sentence has been deleted.

□ Page 3, lines 72-73: here again, you already mention a result of this study in the introduction. Reformulate please.

The sentence has been deleted.

□ Page 3, line 80: data filtering criteria are recommended

“is” has been changed to “are”.

□ Page 4, lines 96-100: rather strange formulation. I would start the sentence with “In the non-linear least square fitting, we consider...” And also, please reformulate “In addition to water vapour” to a more specific formulation as e.g. “the use of spectroscopic water vapour dataset”.

The sentence has been rephrased following the suggestion.

□ Page 4, lines 100-108: to a reader that is not entirely in the satellite data retrieval field, it might seem ought that you start the discussion here with what version 4 is not using (common mode) in

the fitting. Perhaps describe first how the fitting is done with version 4 and then describe the disadvantages of the common mode.

The elements considered in the Version 4.0 nonlinear least square fitting are explained in the previous sentence. The intention of this sentence is to point out the difference with previous versions. For readers who are unfamiliar with common mode, we have added the reference González Abad et al. (2015).

□ Page 4, lines 109-110: as it turned out that the choice of the water vapour reference spectrum really matters for the comparison between the version 3 and 4 TCWV retrievals (later in the manuscript), you might comment on why you use an “older” water vapour reference spectrum in version 4 than in version 3.

We have added a couple of sentences to explain the rationale. It is primarily driven by the validation results. In addition, through personal communication with the HITRAN group at the Smithsonian Astrophysical Observatory, we have recently learned that HITRAN 2016 has some issues with water vapor in the blue wavelength range and that spectroscopic improvements are being made for the next HITRAN release.

□ Page 6, lines 134-139: is the compromise for the wavelength interval as retrieval window for version 4, chosen for a particular orbit number and geographical area, also tested/valid for other orbits and other areas? Please comment.

We have changed “we use OMI Orbit number 10426 ... as an example to ...” to “we randomly selected OMI orbit number 10426 to...”. We tested the result with Orbit 10423 (which cut across the Pacific near the dateline). The patterns exhibited by the variables are similar, though the values for SCD and SCD uncertainties are slightly higher, as Orbit 10423 is over the ocean.

□ Page 6, lines 140-145 and Fig 2.: I really do not understand what is represented in Fig 2. Is this the overall median SCD of the entire dataset or also for the same orbit and geographical area as in Fig. 1? Please specify.

Following the other reviewer’s suggestion, we have combined the original Figure 1 and Figure 2 into one figure. In the figure caption, we have added “for OMI Orbit number 10426”.

□ Page 8, lines 184-185: from which dataset do you obtain the “mean elevation within the corresponding $0.25^\circ \times 0.25^\circ$ grid square”?

The dataset was downloaded from www.temis.nl/data/topo/dem2grid.html in December 2015. The ultimate data source is USGS. A comment about this has been added.

□ Page 9, lines 203-204: “because the fitting includes many other interference molecules whose reference spectra may also contain errors within the retrieval window” □ are version 3 and version 4 not using the same reference spectra for those molecules? So the errors in those reference spectra should then give the same effect in both version 3 and 4, no?

This sentence has been deleted. Version 3 does not include the Vibrational Raman Scattering of air, but Version 4 does. We have recently found, through personal communication with the HITRAN group, that the HITRAN 2016 water vapor spectrum in the blue wavelength range is adversely affected by a line broadening issue. It is therefore not surprising that HITRAN 2008 can lead to lower bias than HITRAN 2016.

□ Page 9, lines 211-212: “This indicates a positive bias of OMI against GPS for small TCWV and a negative bias for large TCWV”

The sentence has been changed following the advice.

□ Page 11, lines 235-236: what might be the reason for the rapid increase of r from $f=0.05$ to $f=0.15$? The other parameters are changing more smoothly between the different f ranges (as well as the r for the other f ranges).

Firstly, the error in cloud top pressure decreases with cloud fraction (Veeffkind et al., 2016). As a result, $f = 0.05$ corresponds to the largest uncertainty in cloud top pressure and the error will propagate to OMI TCWV through AMF, leading to smaller correlation coefficient. Secondly, this is related to the effective dynamical range of TCWV. There is a larger fraction of data pairs with $TCWV > 40$ mm for $f = 0.15$ than for $f = 0.05$. A larger dynamical range generally favors a larger correlation coefficient. The explanation has been added.

□ Page 13, lines 267-268: “suggesting that OMI cloudy TCWV is larger than OMI clear TCWV in general”. Come up with an explanation here.

We have added a sentence to explain. Basically, other things being equal, cloud formation indicates water vapor saturation and therefore higher TCWV than that under clear-sky condition.

□ Page 13, lines 273-274: “In most cases, higher cloud fraction thresholds correspond to larger σ values.” Give an explanation here.

This is consistent with the larger dynamical range (due to a larger fraction of data with high TCWV) for larger cloud fraction thresholds. The relative scatter, however, shows little dependence on cloud fraction threshold. A comment about this has been added.

□ In Section 3.2, you do not compare the version 3 OMI –SSMI TCWV retrievals with the version 4 OMI – SSMI TCWV retrievals. As you did it for GPS (over land), we lack the information of the version 4 behaviour w.r.t. version 3 over the oceans.

We have added the information. Essentially, Version 3 OMI TCWV has significantly larger bias than Version 4.

□ Page 16, lines 348-351: this part belongs to the section describing the sensitivity of the OMI-GPS TCWV differences, and not here.

We mis-typed OMI-SSMIS as OMI-GPS. The error has been corrected. Thanks for catching it.

□ In contrast, I would add a paragraph at the end of section 3 in which you mention the overall conclusions of the OMI TCWV validation with both GPS and SSMIS (e.g. best agreement in the 10-20/30 mm range, worse for smaller & higher TCWV ranges + reasons) and some conclusions on the improvement of version 4 over version 3.

The overall conclusions from the comparisons are summarized in the “Summary and Conclusion” section.

□ Page 17, Fig 7a: indicate the July 2010 and July 2015 epochs on the time series of the ENSO index.

We have drawn dashed vertical lines to indicate the epochs in the plot.

□ Page 17, lines 368-373: mentioning Level 3 and Level 2 for creating the different climatologies is confusing to me. Basically, you first construct the long-term (2005-2015) July TCWV monthly mean map (climatology). Then you create the July 2010 monthly mean map, and the July 2015 monthly mean map and you calculate the differences of those monthly means with the long-term July climatology, right? Shouldn't you use exactly the same dataset (Level 2 or Level 3) for those monthly mean maps?

The procedure described above is indeed what we used for the figure. Averaging the monthly Level 3 July data is an alternative way of composing the July climatology. It does not make any noticeable difference for the purpose of this figure.

□ Page 17, lines 374-377: personally, I would prefer not to use the verbs “increases” and “deceases” when comparing a monthly mean of a specific month with the long-term monthly mean (=anomalies), but rather reserve those verbs in describing trends in time series. I would rather use “is elevated/higher w.r.t. “

We have changed to “higher/lower”.

□ Page 18, line 381: if you give a possible reason for the differences in details, then you should also specify what those “differences in details” are.

We have deleted this part, as it is not essential for this paper. Readers who are interested in the details can compare with Shi et al. (2018).

□ Page 20, line 412: write out NARR.

It has been written out.

▣ Page 20, line 418-419: Describing Figure 9, you write that “TCWV is generally lower in the run without evapotranspiration”. This is true, except in the lower boundaries of the box. Where does it come from?

The higher TCWV in the No ET run near the southern boundary reflects the non-linear water vapor transport from the Gulf region. Note, turning off evapotranspiration not only affects the water vapor flux from the surface, but also influences other meteorological variables, such as temperature and winds. Thus, there is a difference in the water vapor flux across the domain boundary. A comment has been added in the paper.

▣ Page 21, lines 439-448: You use a very detailed description of the AR event of 6-7 Nov 2006, based on datasets that are not used/shown here. Could you not describe the event shorter – process-wise – and refer to the frequently cited Neiman et al. 2008 paper for more details?

We have shortened the description and combined the original Section 4.3.1 and 4.3.2 into one subsection.

▣ Page 22, lines 465-466: “is consistent with the dark stripe in the upper tropospheric water vapor image obtained by GOES-11” □ show similarities to the formation processes, not to datasets or observations not shown here.

We have deleted this part and pointed out that the feature is associated with the same extra-tropical cyclone as the AR is.

▣ Page 24, Figure 11: please add in the figure caption that the grey color coding means no data available.

We have added in the figure caption “Gray color indicates area with no SSM/I data”.

▣ Page 25, line 523-524: specify the “error” in the simulated AR structure (i.e. too strong southern filament of TCWV).

We have specified the error according to the suggestion.

Response to Interactive comment on “OMI Total Column Water Vapor Version 4 Validation and Applications”

by Huiqun Wang et al.

Anonymous Referee #2

In their paper, Wang et al. present an update of a total column water vapor (TCWV) retrieval in the visible spectral range using OMI spectra. They briefly document the changes made for the update and demonstrate the improvements within a validation study including measurements from microwave satellite and ground-based GPS. In addition, they show how the updated data might be used for studies on ENSO, Corn Sweat events, and atmospheric rivers. Overall, the paper is nicely written and easy to read. However I have major concerns regarding the validation study, the drawn conclusions of this study and the case studies of possible applications. I will list my concerns below.

Thanks for the thorough and constructive review. We have revised the paper accordingly. Please find our response to each point below.

Major concerns

- Since this paper presents an update of an existing data set/retrieval, it is evident to clearly demonstrate that the update distinctively improves the algorithm compared to the previous versions. This is not done in this work. Hence I suggest that the authors also include comparisons between the reference data sets and the previous retrieval version.

We have added information for the comparisons between Version 3.0 OMI data and reference TCWV datasets. Essentially, Version 3.0 OMI data have significantly larger bias than Version 4.0.

- I am not fully convinced by the conclusions for the intercomparison between OMI data and GPS data. The linear fit has a slope of 0.82 even for clear-sky observations (radiance cloud fraction < 0.05) and for larger cloud fraction those fit results are actually missing. Additionally, I think that it is a simplification to focus on bias and standard deviation only for interpreting the data. Thus I suggest to include also the mean absolute error (MAE) in the validation study and to perform linear fits for the different cloud fraction thresholds. Furthermore, only some selected scatter plots of the intercomparison between OMI TCWV data and reference data sets are shown in this paper. I suggest that for each cloud fraction threshold the corresponding scatter plots and linear fits are displayed, which may be provided in an Appendix or Supplement to the paper.

Following the suggestion, we have added OMI versus GPS scatter plots for different cloud fraction thresholds. The correlation coefficient and regression line are actually better for cloud fraction $f \geq 0.15$ than for $f = 0.05$. The best regression line has a slope close to one. The linear regression is worse for $f = 0.05$ because of (a) larger error in cloud top pressure in OMCLD02 product for smaller cloud fraction (b) smaller effective dynamical range of TCWV for smaller cloud fraction threshold. Information for the mean absolute error has been added. The MAE is smaller than the standard deviation for the comparisons.

- Although Section 4 shows very interesting insights in the application of the new data set, it does not really fit the scope of AMT and should be skipped. Nevertheless, I think it might be

interesting to see what the impact of other satellite data (AIRS, SSM/I, TES, etc.) will be on the respective case studies and how much better the OMI performs within this comparison. But this will be probably beyond the scope of this paper.

The example applications are intended to show that there is value in the OMI TCWV dataset. In a sense, the applications also serve as an “indirect” validation of the dataset, as a useful dataset is expected to contain well-known signals. As different satellites have different overpass time, resolution and limitation, we believe that each satellite product contributes to the overall understanding of water vapor in its unique way. Comparisons with other satellite datasets for the added value of OMI TCWV are indeed beyond the scope of this paper.

General comments

1. How strong are the cross-correlations between the considered absorption crosssections (more precisely between H₂O, liquid water, glyoxal)? Considering the retrieval fit window, since the 6n+d H₂O line is partially included within this window, do you account for correction factors reported in Lampel et al. (2015)?

The linear correlation coefficient between H₂O and glyoxal is 0.009, and that between H₂O and liquid water is -0.20. The water vapor reference spectrum used in Version 4.0 is based on the original HITRAN 2008 which does not consider the correction in Lampel et al. (2015). A comment about this has been added. The water vapor spectrum in the blue wavelength range is being improved by the HITRAN group. We expect that the next HITRAN release will be better.

2. How large is the dependency on the MERRA-2 water vapor profiles and doesn't this mean that your retrieval is not fully independent from external data sets?

We compared the TCWV computed using the MERRA-2 profiles with those computed using the ERA-Interim profiles for July 2006. The result shows that the standard deviation of the difference can be significant (~ 3mm). The information has been added to the text. To mitigate the dependence of TCWV on external datasets, scattering weights are provided in the Level 2 OMI product. Users can convolve the scattering weights with the profiles of their choice to calculate AMF and adjust TCWV.

3. It would be very interesting to the reader to see which update step contributes most to the improvement (new fit window, new cloud product, new MERRA-2 data?).

Between Version 3.0 and 4.0, the reference water vapor spectrum leads to the largest difference. This is mentioned when we discuss supplementary Figure 1.

4. Do you use the radiative or the geometric cloud fraction? The cloud fraction criterion of 0.05 seems very restrictive to me. What fraction of OMI data is filtered by this criterion?

We used the cloud fraction reported in the OMCLDO2 product (Veefkind et al., 2016). We have clarified this in the revised paper. In Veefkind et al. (2016), this effective cloud fraction is calculated using the reflectance at the top-of-atmosphere, for the clear part and for the cloudy part, and can be considered as a radiative cloud fraction.

On a typical day (July 1, 2016), among the OMI data that pass the MDQFL and TCWV range test, $f < 0.05$ accounts for about 35% of the data. The information has been added.

5. Linear regression for land data: Why is the slope so bad? Please discuss in more detail the uncertainties of the SCD and the AMF.

This is related to the relatively large bias for $TCWV < 10$ mm. The slope improves if these data pairs are excluded from the linear regression. A comment about this has been added. Moreover, the slope is also due to the smaller dynamical range of TCWV for cloud fraction < 0.05 . For larger cloud fraction thresholds, there is a larger fraction of data pairs with higher TCWV values, and the regression slopes improve. The best regression line has a slope close to one (for cloud fraction < 0.25 or 0.35). A figure has been added to show this.

Typical uncertainties of SCD can be found in Figure 1 and supplementary Figure 1. For the uncertainty related to gas profiles for AMF, please see our reply to (2). For the uncertainty related to scattering weights for AMF, we have conducted error propagation analysis for a typical orbit, results show that most AMF error is $< 3\%$, though it can be up to 15% for cloudy pixels over land. The information has been added in Section 2.

6. El Nino study: Since you only consider clear-sky observations, your averaged data are biased. How strong is thus the influence/impact of clouds?

For the El Niño study, we used cloud fraction < 0.15 and cloud top pressure > 750 hPa to filter OMI data (in addition to other usual criteria). This choice is based on the validation results presented previously. Using stricter criteria for clouds will result in lots more missing data in the map, using less restrictive criteria for clouds will incur larger data bias which will be hard to disentangle from the signal. Thus, the influence of clouds on the pattern is not discussed in this paper.

7. Corn Sweat study: Do you observe the increase of TCWV also in the GPS data?

Yes. Several GPS stations over the area observed an increase of TCWV during the event, though coincident OMI data at the particular stations are not found. Supplementary figure has been added.

8. AR study: I do not see the benefit of the description of the AR in Section 4.3.2, especially when this AR is already analysed in detail by Neimann et al. (2008). So the authors might think about skipping this section.

We have shortened the description of this event and merged the original Section 4.3.1 and 4.3.2 into one subsection.

Specific comments

- line 10: please introduce the complete name for OMI (Ozone Monitoring Instrument)
We have added the complete name.
- line 12: „various updates“ _ more specific (e.g. updated cloud product, etc.)

We have changed “various updates” to “reference spectra and gas profiles”.

- line 16: geometric/radiative cloud fraction?

It is the effective cloud fraction reported in the OMCLDO2 product (Veefkind et al., 2016). It is based on radiances and therefore can be considered as a radiative cloud fraction. A sentence about this has been added to clarify.

- line 22: I think you meant 20-30 instead of 10-30 mm

A change has been made to summarize the result more accurately.

- line 27: atmospheric river

It has been changed following the suggestion.

- line 37: in situ

It has been changed following the suggestion.

- line 38: „ground“ instead of surface

It has been changed following the suggestion.

- line 41: the reference is Schröder et al. (2018)

It has been corrected.

- line 43: I would rather say clear-sky and cloudy-sky

It has been changed following the suggestion.

- line 58: It is very unusual to mention results already in the introduction

The sentence has been deleted.

- line 69: reference spectra for water vapor from the latest HITRAN database . . .

It has been changed following the suggestion.

- line 74: please insert a line break

A line break has been inserted.

- line 86: Aura

It has been changed following the suggestion.

- line 88: 1:30 PM local time (this is actually the equator crossing-time)

It has been changed to “1:30 PM equator crossing time”.

- line 95: The specifics of Version 4 are discussed . . .

It has been changed following the suggestion.

- line 106: show

It has been changed following the suggestion.

- line 125: „smaller toward the the lower right corner of the domain“ please rephrase this

The sentence has been rephrased to be more specific about what the lower right corner of the domain means.

- line 131: „ 5×10^{23} molecules/cm²“ where is this value coming from?

The threshold corresponds to a SCD of about 149.45 mm. It is meant to filter out large outliers. For reference, the largest TCWV of the GPS and SSMIS datasets (Section 3) is about 75 mm. At low latitudes where TCWV is high, more than 90% of the AMFs are between 0.5 and 2.0. We have added the information to the text.

- line 134: Shouldn't the residual be small as well as not contain any structures, i.e. it should be noisy?

We have changed “reduce the residual” to “reduce the residual's amplitude and structure”.

- line 159: influence the AMF

It has been changed following the suggestion.

- line 168 to 172: it would be very helpful to have a map showing the distribution of the GPS stations.

We have added (Wang et al., 2016) as a reference for the distribution of the stations on a map.

- line 176: what are unphysical values? Please describe in more detail.
We have changed it to “negative or extremely large (TCWV > 75 mm) values”.
- line 180: the time window seems quite large, since water vapor can vary a lot during day. I think it would be better reduce the time range to plus/minus 1.5 hours.
We have changed the time window to 1200 LT - 1500 LT.
- line 185: which elevation database are you using?
The 0.25°×0.25° topography was downloaded from www.temis.nl/data/topo/dem2grid.html.
- line 186: „we consider the OMI and GPS data that are less than 75 mm.“ why not higher values (e.g. 100 mm)?
The largest TCWV of the GPS data used is about 75 mm. A comment about this has been added.
- line 195 and 196: the references have to be switched
The references have been switched. Thanks for catching that.
- line 209: please provide R² of the linear fit
It has been provided.
- line 279: Isn't this also an instrumental issue (poor signal to noise ratio of OMI?)
We have rephrased in term of “low signal-to-noise ratio when TCWV < 10 mm in the OMI retrieval”.
- line 290: cycles
It has been deleted.
- line 291: which special cases?
This part of the sentence has been deleted. Users who are interested in the details can refer to [Diedrich et al. \(2016\)](#).
- line 293 to 295: now you are using different requirements for the fit (e.g. higher TCWV threshold).
We have changed the data filtering criteria so that they are consistent with the ones used before. The corresponding figures and discussions have also been updated as needed.
- line 373: Figure 7cd _ Figure 7c) and 7d)
We have made the change.
- line 376 and 377: decrease
Following the other reviewer's suggestion, we have changed increase/decrease to higher/lower.
- line 492: what is the weight of the OMI observations for your assimilated data? Can you provide a map for that?
The weight varies for each simulation window depending on the data quality and data density. A single map cannot describe the process, therefore, it is not provided in the paper.
- line 556: „we recommend to consider only OMI data ...“
The change has been made.
- Table 3: Please indicate the fraction of used data points to available data points in percent. Also split up the regression column into slope and intercept and coefficient of determination (R²).
We have made the changes.
- Figure 1: please remove panel d) and replace it with Figure 2
We have made the change.
- Figure 3: Please include a comparison for Version 3 and the linear fits in the scatter plots. Also colorbar in the bottom panel has no labels.

We have fixed the color bar. We have included the comparisons for Version 3 OMI in the text. Given the focus and length of this paper, we feel that it is not essential to include scatter plots for Version 3.

- Figure 10: Please zoom into the region of interest.

We have made the change.

- Figure 12: Why does the model simulate rainfall in the northwest of Oregon even for the case with assimilated OMI data?

Admittedly, even with data assimilation, the model is still not perfect. Errors in both the model and the data, as well as the amount and distribution of the data, contribute to the error in the assimilation result. For the example in Figure 12, we are glad to see that the model does a better job within the red box when OMI data are used. A detailed investigation of the assimilation error is beyond the scope of this paper. A comment about this has been added.

References

- Lampel, J., et al. "On the relative absorption strengths of water vapour in the blue wavelength range." *Atmospheric Measurement Techniques* 8.10 (2015): 4329-4346.
- Neiman, Paul J., et al. "Meteorological characteristics and overland precipitation impacts of atmospheric rivers affecting the West Coast of North America based on eight years of SSM/I satellite observations." *Journal of Hydrometeorology* 9.1 (2008): 22-47.
- Schröder, Marc, et al. "The GEWEX Water Vapor Assessment archive of water vapour products from satellite observations and reanalyses." *Earth System Science Data* 10.2 (2018): 1093-1117.

Thanks for providing the references. We have added them in the paper.

1 OMI Total Column Water Vapor Version 4 Validation and Applications

2 Huiqun Wang¹, Amir Hossein Souri¹, Gonzalo González Abad¹, Xiong Liu¹ and Kelly Chance¹

3 ¹. Smithsonian Astrophysical Observatory, 60 Garden Street, Cambridge, Massachusetts 02138,
4 USA

5
6 *Correspondence to: Huiqun (Helen) Wang (hwang@cfa.harvard.edu)*

7 **Abstract**

8
9 Total Column Water Vapor (TCWV) is important for the weather and climate. TCWV is
10 derived from the [Ozone Monitoring Instrument](#) (OMI) visible spectra using the Version 4.0
11 retrieval algorithm developed at the Smithsonian Astrophysical Observatory. The algorithm uses
12 a retrieval window between 432.0 and 466.5 nm and includes ~~various updates~~ [to reference](#)
13 [spectra and water vapor profiles](#). The retrieval window optimization results from the trade-offs
14 among competing factors.

15 ___ The OMI product is characterized by comparing against commonly used reference datasets –
16 [Global Positioning System](#) (GPS) network data over land and [Special Sensor Microwave Imager](#)
17 [/ Sounder](#) (SSMIS) data over the oceans. We examine how cloud fraction and cloud top pressure
18 affect the comparisons. The results lead us to recommend filtering OMI data with cloud fraction
19 [less than \$f = 0.05 - 0.25\$](#) and cloud top pressure > 750 mb (or stricter), in addition to the data
20 quality [flag](#), fitting RMS and TCWV range check. [Over land, for \$f = 0.05\$, the overall mean of](#)
21 [\(OMI-GPS\) is \$0.32\$ mm with a standard deviation \(\$\sigma\$ \) of \$5.2\$ mm, \[the smallest bias occurs when\]\(#\)
22 \[TCWV = \\$10 - 20\\$ mm, and the best regression line corresponds to \\$f = 0.25\\$; Over the oceans, for \\$f\\$\]\(#\)
23 \[= \\$0.05\\$, the overall mean of \\(OMI-SSMIS\\) is \\$0.4\\$ mm \\(\\$1.1\\$ mm\\) with \\$\sigma = 6.5\\$ mm \\(\\$6.8\\$ mm\\) for\]\(#\)
24 \[January \\(July\\), the smallest bias occurs when TCWV = \\$20 - 30\\$ mm, and best regression line\]\(#\)
25 \[corresponds to \\$f = 0.15\\$. For both land and the oceans,\]\(#\) the difference between OMI and the
26 reference datasets is relatively large when TCWV is less than 10 mm. The bias for Version 4.0
27 OMI TCWV is much smaller than that for Version 3.0.](#)

28 As test applications of the Version 4.0 OMI TCWV over a range of spatial and temporal
29 scales, we find prominent signals of the patterns associated with El Niño and La Niña, the high

30 humidity associated with a corn sweat event and the strong moisture band of an [atmospheric](#)
31 [river \(AR\)](#). A data assimilation experiment demonstrates that the OMI data can help improve [the](#)
32 [Weather Research and Forecasting model](#) (WRF)'s skill at simulating the structure and intensity
33 of the AR and the precipitation at the AR landfall.

34 **1 Introduction**

35 Water vapor is of profound importance for weather and climate. Through condensation, it
36 forms clouds that modify albedo, affect radiation and interact with particulate matter. In addition,
37 latent heat released from water vapor condensation can influence atmospheric energy budget and
38 circulation. Water vapor is the most abundant greenhouse gas, accounting for ~50% of the
39 greenhouse effect (Schmidt et al., 2010). Thus, monitoring the spatial and temporal distributions
40 of water vapor is crucial for understanding water-vapor related processes.

41 Water vapor has been measured using a variety of [in_situ](#) and remote sensing techniques from
42 the [ground](#), air and space. Satellite data provide global perspective and are indispensable for
43 constraining reanalysis products (Dee et al., 2011; Gelaro et al., 2017). The current satellite
44 water vapor datasets are evaluated through the Global Energy and Water cycle Exchanges
45 (GEWEX) Water Vapor Assessment program (Schröder et al., [2019](#)). These datasets are derived
46 from visible, near infrared (NIR), Infrared (IR), microwave and [Global Positioning System](#)
47 [\(GPS\)](#) measurements. Each dataset has its own characteristics [and contributes to the](#)
48 [understanding of water vapor in its own way](#). For example, microwave data are useful for both
49 [clear-sky](#) and [cloudy-sky](#) conditions, but are best suited for non-precipitating ice-free oceans due
50 to the complications associated with land surface emissivity; NIR data are best suited for the
51 land, as the surface albedo is low over the oceans; IR data are available over all surface types,
52 but are strongly influenced by clouds and less sensitive to the planetary boundary layer; visible
53 data are sensitive to the boundary layer over both land and the oceans, but are complicated by
54 uncertainties in clouds and aerosols (Wagner et al., 2013).

55 Total Column Water Vapor (TCWV, also called Integrated Water Vapor - IWV, or
56 Precipitable Water Vapor - PWV) can be retrieved from the [7v](#) water vapor vibrational polyad
57 [band](#) (around 442 nm) despite the weak absorption (Wagner et al., 2013). This made it possible
58 to derive TCWV from instruments measuring in the blue wavelength range. Since water vapor is
59 a weak absorber here, saturation of spectral lines is not of concern (Noël et al., 1999). Moreover,

60 the similarity between the land and ocean surface albedo in the blue wavelength range suggests a
61 roughly uniform sensitivity of the measurement over the globe (Wagner et al., 2013). However,
62 weaker absorption tends to result in larger relative uncertainties, especially for low TCWV
63 amount. ~~As an example, for the Version 4 retrieval investigated in this paper, when TCWV is~~
64 ~~greater than 10 mm, the medium fitting uncertainty is 10–15%, but for TCWV less than 10 mm,~~
65 ~~it rises to 40–50%.~~

66 Using the visible spectra measured by the Ozone Monitoring Instrument (OMI), Wang et al.
67 (2014) retrieved Version 1.0 TCWV from 430 – 480 nm and publically released the data on the
68 Aura Validation Data Center (AVDC, <https://avdc.gsfc.nasa.gov>). Wang et al. (2016) found that
69 the Version 1.0 data generally agree with ground-based GPS data over land, but are significantly
70 lower than the microwave observations over the oceans. They found that using a narrower
71 retrieval window (427.7 – 465 nm) in Version 2.1 could improve the data over the oceans
72 without adversely affecting the results over land much. However, the Version 2.1 data were only
73 generated for a few test months and not released to the public. An interim Version 3.0 OMI
74 TCWV product is available at AVDC. Compared with Version 2.1, Version 3.0 uses the
75 reference spectrum for water vapor [from the latest HITRAN database](#) (Gordon et al., 2016) and
76 that for liquid water from Mason et al. (2016), as well as the newest cloud product (Veefkind et
77 al., 2016). The Version 3.0 retrieval window (427.0 – 467.0 nm) is adjusted from that for
78 Version 2 within 2 nm on each end based on fitting uncertainty for a randomly selected test orbit.
79 ~~However, as discussed later, we find that the Version 3 data show much larger bias than the~~
80 ~~latest Version 4.~~

81 This paper focuses on Version 4.0 OMI TCWV which [has replaced](#) Version 3.0 on AVDC.
82 We present the Version 4.0 retrieval algorithm which incorporates a more vigorous systematic
83 optimization for the retrieval window and miscellaneous updates. We characterize the
84 performance of the Version 4.0 dataset by comparing with well-established references, such as
85 the GPS network data and the [Special Sensor Microwave Imager / Sounder](#) (SSMIS)
86 observations. We also assess the performance of Version 4.0 against that of Version 3.0. To
87 provide practical guide to users of the new data, we investigate the influence of cloud fraction
88 and cloud top pressure on the comparisons. Based on the results, data filtering criteria [are](#)
89 recommended. As an additional check on the Version 4.0 product, we show test applications of
90 the data to a range of spatial and temporal scales, including El Niño / La Niña, a corn sweat

91 event and an atmospheric river (AR) event. For the first time, a data assimilation experiment for
92 the AR event demonstrates that the OMI TCWV data can provide useful constraint for weather
93 prediction.

94 **2 Retrieval Algorithm**

95 OMI on board the [Aura](#) spacecraft is a UV/Visible imaging spectrometer (Levelt et al.,
96 2006). It has been making daily global observations at a nominal 13×24 km nadir resolution
97 [from a 1:30 PM equator crossing time polar orbit](#) since October 2004. The UV-Visible channel
98 of OMI covers 350-500 nm at a spectral resolution of about 0.5 nm.

99 TCWV is derived from the OMI visible spectrum using a commonly used two-step approach.
100 First, the Slant Column Density (SCD, molecules/cm²) is retrieved from a spectral fitting
101 algorithm. Then, the Vertical Column Density (VCD, molecules/cm²) is calculated from the ratio
102 of SCD and Air Mass Factor (AMF) (Palmer et al., 2001). VCD can be converted to TCWV
103 using 10²³ molecules/cm² = 29.89 mm. The details of the two-step procedure can be found in
104 González Abad et al. (2015). The specifics of Version 4.0 [are](#) discussed below.

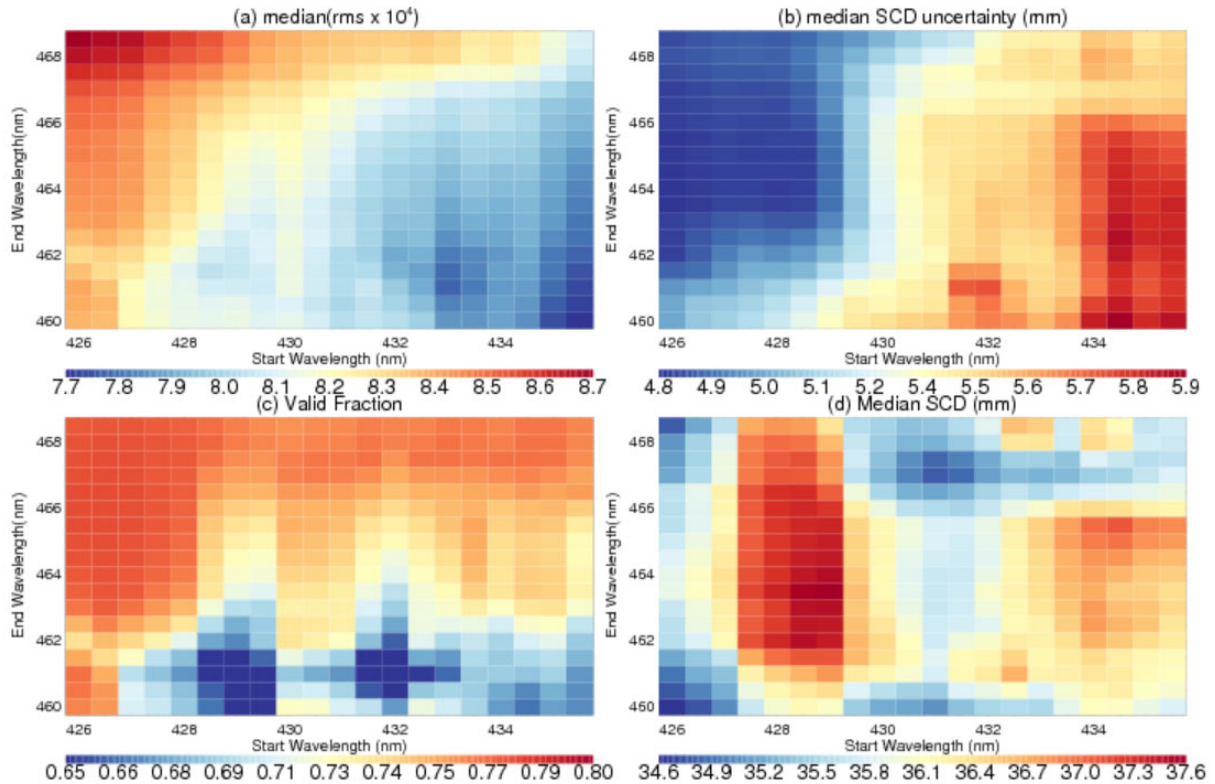
105 The Version 4.0 spectral fitting parameters are summarized in Table 1. [In the nonlinear least](#)
106 [square fitting](#), we consider wavelength shift, under-sampling, closure polynomials (3rd order
107 multiplicative and additive), [reference spectroscopic spectra of water vapor](#), interfering
108 molecules (O₃, NO₂, O₄, liquid water, C₂H₂O₂ and IO) and Raman scattering (the Ring effect,
109 vibrational Raman scattering of air and the water Ring effect). In comparison with previous
110 versions, Version 4.0 no longer fits common mode (i.e. the mean of the fitting residual, [González](#)
111 [Abad et al., 2015](#)). It turns out that the common mode for land is different than that for ocean
112 (Wang et al., 2014). Previous retrievals derive a common mode for each orbit swath using the
113 pixels in the low latitudes which often includes both land and ocean scenes. Thus, the derived
114 common mode depends on the proportion of land versus ocean pixels of the spacecraft orbit and
115 is not universally suitable for all the pixels of the swath. Statistics for Orbit 10423 show that
116 although the mean of SCD differs little between the retrievals with and without common mode in
117 the fitting (0.1 mm), the standard deviation of SCD between them can be significant (1.7 mm).
118 Most of the settings in Table 1 are shared between Version 3.0 and 4.0, except that Version 3.0
119 uses [HITRAN 2016](#) (Gordon et al., 2016) as the water vapor reference spectrum, includes
120 common mode in the fitting, but does not consider vibrational Raman scattering of air (Lampel et

121 al., 2015a). We revert to the HITRAN 2008 water vapor spectrum (Rothman et al., 2009) in
 122 Version 4.0 because validation results show that it leads to better agreements with the GPS and
 123 SSMIS TCWV data (Section 3). We did not apply the correction of Lampel et al. (2015b) to the
 124 HITRAN 2008 water vapor spectrum. It is recently found that HITRAN 2016 is adversely
 125 affected by an issue with line broadening for water vapor in the blue wavelength range and
 126 improvements are being made for the next HITRAN release (the HITRAN group, personal
 127 communication).

128 **Table 1.** Parameters used in Version 4.0 spectral fitting for OMI total column water vapor.

Wavelength shift	Solar reference spectrum	Dobber et al. (2008)
Target	H ₂ O	288K, Rothman et al. (2009)
Interference molecules	O ₃	228K, Brion et al. (1993)
	NO ₂	220K, Vandaele et al. (1998)
	O ₄	293K, Thalman and Volkamer (2013)
	Liquid water	Mason et al. (2016)
	C ₂ H ₂ O ₂	296K, Volkamer et al. (2005)
	IO	298K, Spietz et al. (2005)
Raman scattering	Ring effect	Chance and Spurr (1997)
	Water Ring	Chance and Spurr (1997)
	Air Vibrational Raman	Lampel et al. (2015a)
Other	Additive polynomial	3 rd order
	Multiplicative polynomial	3 rd order
	Under-sampling	Chance et al. (2005)

129
 130 To optimize the retrieval window, we randomly selected OMI Orbit number 10426 (on July
 131 1, 2006) to examine the effect of varying the starting and ending wavelengths around the 7v
 132 water vapor absorption band. The orbit swath contains 60×1644 ground pixels and covers parts
 133 of Australia, the Pacific, China and other areas. We systematically adjust the starting wavelength
 134 within 426.0-435.0 nm and the ending wavelength within 460.0-468.5 nm, both at 0.5 nm steps.



135

136

Figure 1. Sensitivity of the retrieval to the start and end wavelengths (nm) of the retrieval window for OMI Orbit number 10426. (a) Median of fitting RMS $\times 10^4$; (b) median of water vapor SCD fitting uncertainty in mm; (c) valid fraction for retrievals; (d) median SCD in mm.

138

139

In previous versions, the fitting window is selected based on the fitting uncertainty (Wang et al., 2014, 2016). For Version 4.0, we consider the following four factors. (1) Figure 1a shows that the median of the fitting Root Mean Squared error (RMS) is smaller toward the lower right corner of the domain (i.e., longer start wavelength and shorter end wavelength); (2) Figure 1b shows that the medium fitting uncertainty of water vapor SCD decreases toward the upper left corner; (3) Figure 1c shows that the fraction of valid retrievals for the orbit generally increases toward the upper part of the domain. Valid retrievals here refer to those that pass the main data quality check (MDQFL = 0) and have positive SCDs. The main data quality check ensures that the fitting has converged, the SCD is $< 5 \times 10^{23}$ molecules/cm² (149.45 mm) and within 2σ of the fitting uncertainty. The SCD threshold here is meant to filter out large outliers. For reference, the largest TCWV of the GPS and SSMIS datasets used in Section 3 is about 75 mm. At low latitudes where TCWV is large, more than 90% of the OMI AMFs are between 0.5 and 2.0; (4) The length of the retrieval window increases with the difference between the end and start

140

141

142

143

144

145

146

147

148

149

150

151

wavelengths. The general patterns exhibited by Orbit number 10426 in Figure 1 also hold for Orbit number 10423 which cuts across the Pacific near the dateline.

Ideally, we would like to have small fitting RMS to reduce the residual's amplitude and structure, a small fitting uncertainty to reduce error, a large fraction of valid data to increase data volume and a long retrieval window to include more information into the fitting. However, these criteria cannot be met simultaneously. As a compromise, we select the wavelength interval between 432.0 nm and 466.5 nm as the retrieval window for Version 4.0. For Orbit number 10426, this leads to a median fitting RMS of 8.1×10^{-4} , a median SCD uncertainty of 5.4 mm, a valid fraction of 0.75 and a window length of 34.5 nm (Figure 1). Figure 1d shows that the median SCD for Orbit number 10426 varies between 34.6 mm and 37.6 mm. This 3 mm difference corresponds to an 8% variation and exhibits a complex pattern within the domain. The Version 4.0 retrieval window leads to a median SCD of 35.5 mm for Orbit number 10426 which is near the beginning of the middle third of the SCD range. The ratio between the median SCD uncertainty and the median SCD (i.e., the relative SCD uncertainty) is about 0.15. Note that this value is for the whole orbit which includes a wide range of SCDs. As shown in Supplementary Figure 1, the relative SCD uncertainty is >1.2 for SCD = 0 – 10 mm, drops to about 0.4 for SCD = 10 – 20 mm, and to about 0.1 for SCD > 40 mm.

The AMF is calculated by convolving scattering weights with the shape of water vapor vertical profile (González Abad et al., 2015). The scattering weight is interpolated from the same look-up table as that used in Wang et al. (2016). The scene specific information used in the AMF calculation is listed in Table 2. By propagating typical errors for surface albedo (15%), cloud fraction (10%) and cloud top pressure (15%), we find that the AMF error for a typical orbit (number 10426) is mostly < 3%, though for cloudy pixels over land, the AMF error can be up to 15%. Version 4.0 uses the $0.5^\circ \times 0.667^\circ$ monthly mean MERRA-2 water vapor profile (Gelaro et al., 2017) for the month and year corresponding to the retrieval, while previous versions used the monthly mean of 2007 for all years. To evaluate the error associated with gas profiles, we compare the TCWV calculated using the daily MERRA-2 profile against that calculated using the monthly MERRA-2 profile for July 2006 (for TCWV within the 0 – 75 mm range). Results show that TCWV(daily) – TCWV(monthly) has a mean (median) of 0.3 mm (0 mm) with a standard deviation of 5.0 mm. When comparing the TCWV calculated using the daily MERRA-2 profile against that calculated using the daily ERA-Interim profile for July 2006, we find that

183 [TCWV\(MERRA-2\) – TCWV\(ERA-Interim\)](#) has a mean (median) of -0.1 mm (0 mm) with a
 184 [standard deviation of 2.8 mm. Thus, gas profiles can introduce substantial scatter to the retrieved](#)
 185 [TCWV](#). AMF is highly sensitive to clouds (Wang et al., 2014; Vasilkov et al., 2017). Version 4.0
 186 uses the cloud information from Veefkind et al. (2016). The primary difference with the Acarreta
 187 et al. (2004) cloud product used in Version 1.0 and 2.1 is in the cloud top pressure for cloud
 188 fraction $f < 0.3$. In addition to the factors in Table 2, aerosol and surface bi-directional
 189 reflectance distribution function (BRDF) influence the AMF (Lorente et al., 2017; Vasilkov et
 190 al., 2017), but have not been considered in the retrieval yet.

191 **Table 2.** Parameters used in AMF calculation

Solar Zenith Angle	OMI L1B data
View Zenith Angle	
Relative Azimuth Angle	
Surface Albedo	OMLER (Lambert equivalent reflectance) Kleipool, et al. (2008)
Cloud fraction	OMCLDO2 (derived from O ₂ -O ₂) Veefkind et al. (2016)
Cloud top pressure	
Surface pressure	MERRA-2 monthly data (0.5°×0.667°), Gelaro et al. (2017)
Water vapor profile	

192

193 3 Validation

194 To validate the Version 4.0 OMI TCWV data, we compare them against two commonly used
 195 reference datasets – a GPS network dataset for land and a microwave dataset for the oceans.

196 3.1 OMI and GPS over land

197 To assess the Version 4.0 OMI TCWV over land, we compare against the GPS network data
 198 downloaded from NCAR (rda.ucar.edu/datasets/ds721.1). The GPS data are composed of 2-
 199 hourly TCWV at International GNSS Service (IGS), SuomiNet and GEONET stations, and have
 200 an estimated error of < 1.5 mm (Wang et al., 2007; Ning et al., 2016). The subset of IGS-
 201 SuomiNet data for the whole year of 2006 is used in this paper. [The geographical distribution of](#)
 202 [the stations can be found in Wang et al. \(2016\)](#). Most of the stations are concentrated in North
 203 America and Europe, fewer are scattered on other continents.

204 OMI TCWV data are filtered using the following criteria. The stripes in Level 2 swaths due
 205 to systematic instrument error are removed using the SCD scaling procedure described in Wang

206 et al. (2016). The pixels affected by OMI's row anomaly are filtered out
207 (projects.knmi.nl/omi/research/product/rowanomaly-background.php), as well as unphysical
208 negative or extremely large (i.e., TCWV > 75 mm) values. For the clear-sky comparison in
209 Figure 3, we require cloud fraction < 5% and cloud top pressure > 750 mb, in addition to
210 MDQFL = 0 and fitting RMS < 0.001. The cloud fraction and cloud top pressure are from the
211 OMCLDO2 cloud product (Veefkind et al., 2016) and are included in the Level 2 OMI product
212 for ease of data filtering. On a typical day of (July 1, 2006), among the OMI data that pass the
213 MDQFL and TCWV range test, cloud fraction < 0.05 accounts for 35% of the data, cloud top
214 pressure > 750 mb accounts for 53% of the data and RMS < 0.001 accounts for 72% of the data.

215 To co-locate GPS and OMI data, we select the GPS data observed between 1200 LT and
216 1500LT. This 3-hour local time range covers the OMI overpass time. We average the qualified
217 OMI data within 0.25° longitude × 0.25° latitude of the GPS stations for each day. To minimize
218 the influence of local topography (e.g., mountain peaks, river valleys), if a station's elevation is
219 more than 250 m different than the mean elevation within the corresponding 0.25°×0.25° grid
220 square, then it is excluded from the analysis. The 0.25°×0.25° topography was downloaded from
221 www.temis.nl/data/topo/dem2grid.html. The comparison between OMI and GPS is made for
222 TCWV within the range of 0 – 75 mm as the largest TCWV for the GPS data is about 75 mm.
223 The co-locating procedure leads to about 11,000 co-located data points for the entire year of
224 2006.

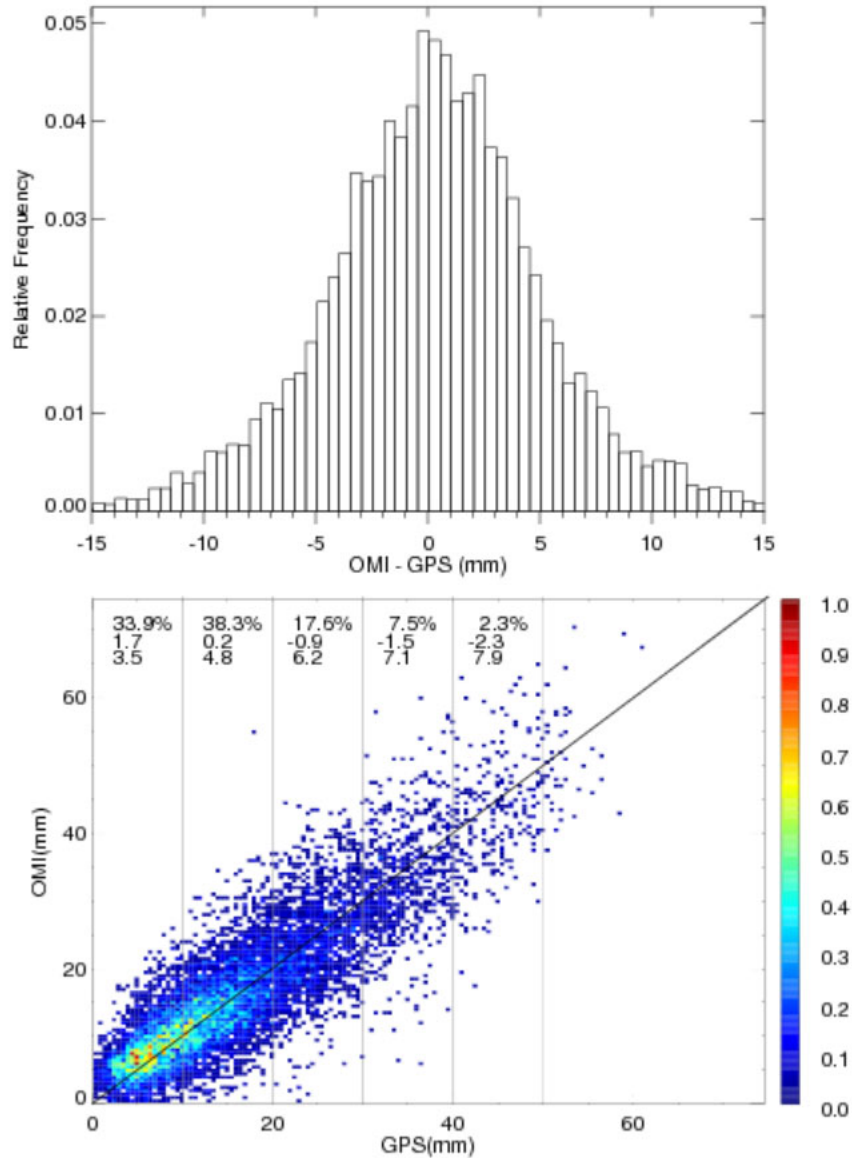
225 Figure 2 shows the comparison between the resulting co-located GPS and Version 4 OMI
226 TCWV. The top panel shows the histogram of OMI-GPS (in 0.5 mm bins). The bin from -0.5 to
227 0.0 mm corresponds to the peak of the distribution. The overall mean (median) of OMI-GPS is
228 0.32 mm (0.35 mm), with a standard deviation of 5.2 mm. The mean (median) absolute error is
229 3.9 mm (3.0 mm).

230 The bottom panel of Figure 2 shows the joint distribution of the co-located GPS and Version
231 4.0 OMI data. The count for each 0.5 mm bin is normalized by the maximum of all bins. About
232 34% of the data have TCWV < 10 mm, 72% have TCWV < 20 mm and 90% have TCWV < 30
233 mm. There is a general linear correlation between GPS and OMI data, with a correlation
234 coefficient of $r = 0.87$ ($R^2 = 0.76$). The linear regression line ($\text{OMI} = 2.22 + 0.88 * \text{GPS}$, where
235 OMI and GPS TCWV are in mm) has a significant positive intercept and a slope that is less than

236 one. This indicates a positive bias of OMI against GPS for small TCWV and a negative bias for
237 large TCWV. Indeed, as indicated at the top of the panel, the mean of OMI-GPS for each 10 mm
238 GPS TCWV bin decreases from 1.7 mm for TCWV = 0 – 10 mm to -2.3 mm for TCWV = 40 –
239 50 mm, though the fraction of data for TCWV > 40 mm is < 3%. The corresponding standard
240 deviation (σ) increases from 3.5 mm to 7.9 mm. The minimum bias of 0.2 mm occurs for TCWV
241 in the 10 – 20 mm bin. The large positive bias of the 0 – 10 mm bin (as compared with the
242 TCWV of the bin) has significant adverse effect on the regression line. For TCWV > 10 mm, the
243 regression line ($OMI = 1.51 + 0.91 \times GPS$) is better.

244 In comparison, although Version 3.0 OMI is similarly correlated with GPS (correlation
245 coefficient $r = 0.86$), it has a much larger positive bias of 2.8 mm (with a standard deviation of
246 5.5 mm). The large bias is attributed to the much larger SCD of Version 3.0 (Supplementary
247 Figure 2b), as the AMFs of both versions roughly follow the 1:1 line (Supplementary Figure 2a).
248 Sensitivity tests show that the larger Version 3.0 SCD is primary due to the water vapor
249 reference spectrum. If the water vapor reference spectrum in Version 4.0 is replaced with that of
250 Version 3.0 (Test 1), then the median SCD increases by about 4.5 mm for Orbit 10423
251 (Supplementary Figure 2c). Modifying the retrieval window for Version 3.0 cannot sufficiently
252 reduce the retrieved SCD, therefore cannot make significantly better agreement with the
253 reference TCWV data. As Version 4.0 shows better performance, this paper focuses on
254 characterizing Version 4.0 to provide useful information to potential users. In subsequent
255 discussions, OMI data refer to Version 4.0 unless specified otherwise.

256



257

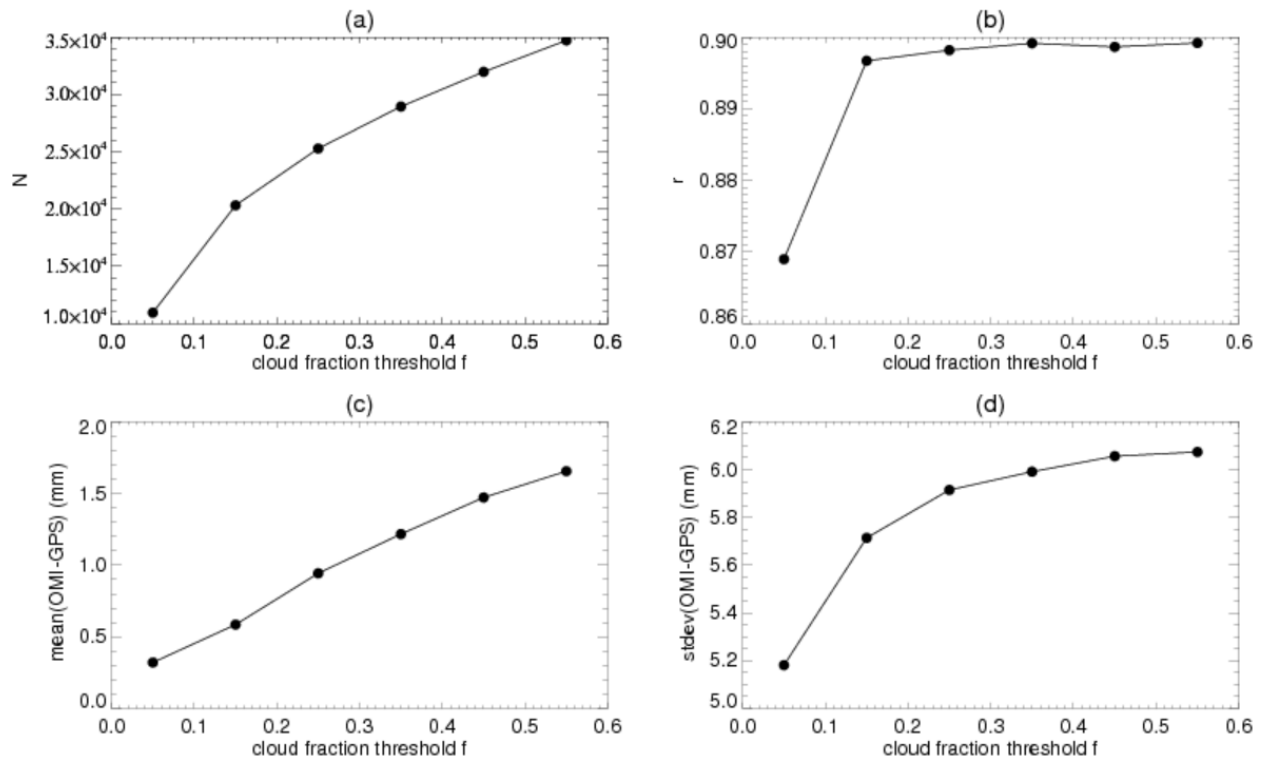
258 **Figure 2.** Comparison between co-located GPS and OMI TCWV (mm) for all days in 2006. The
 259 data filtering criteria include cloud fraction < 5%, cloud top pressure > 750 mb, and others
 260 discussed in the text. (Top) Relative frequency of occurrence for OMI-GPS (mm). (Bottom)
 261 Normalized joint distribution of GPS versus OMI TCWV (mm). The three lines of text from top
 262 to bottom indicate the percentage of data points (1st), the mean of OMI-GPS in mm (2nd), and
 263 the standard deviation of OMI-GPS in mm (3rd) for each 10 mm GPS TCWV, respectively. The
 264 1:1 is plotted for reference.

265

266 OMI TCWV retrieval is highly sensitive to clouds (Wang et al., 2014). In Figure 3, we
267 examine the effect of OMI cloud fraction threshold (f) on the comparison while keeping other
268 data filtering criteria the same as those for Figure 2 (i.e., cloud fraction $< f$, cloud top pressure $<$
269 750 mb, MDQFL = 0, fitting RMS < 0.001 and $0 < \text{TCWV} < 75$ mm). From $f = 0.05$ to $f = 0.55$,
270 the number of co-located data pairs (N) more than triples, the mean of OMI-GPS increases from
271 0.32 mm to 1.66 mm, the standard deviation of OMI-GPS increases from 5.2 mm to 6.1 mm. The
272 linear correlation coefficient (r) increases from $r = 0.87$ at $f = 0.05$ to $r \simeq 0.90$ at $f = 0.15$, then
273 levels off for larger cloud fraction thresholds. It should be noted that the error in cloud top
274 pressure decreases with cloud fraction in the OMCLDO2 product (Veefkind et al., 2016). As a
275 result, $f = 0.05$ corresponds to the largest uncertainty in cloud top pressure, and the error will
276 propagate into OMI TCWV through AMF, leading to smaller correlation coefficient than those
277 for larger f values.

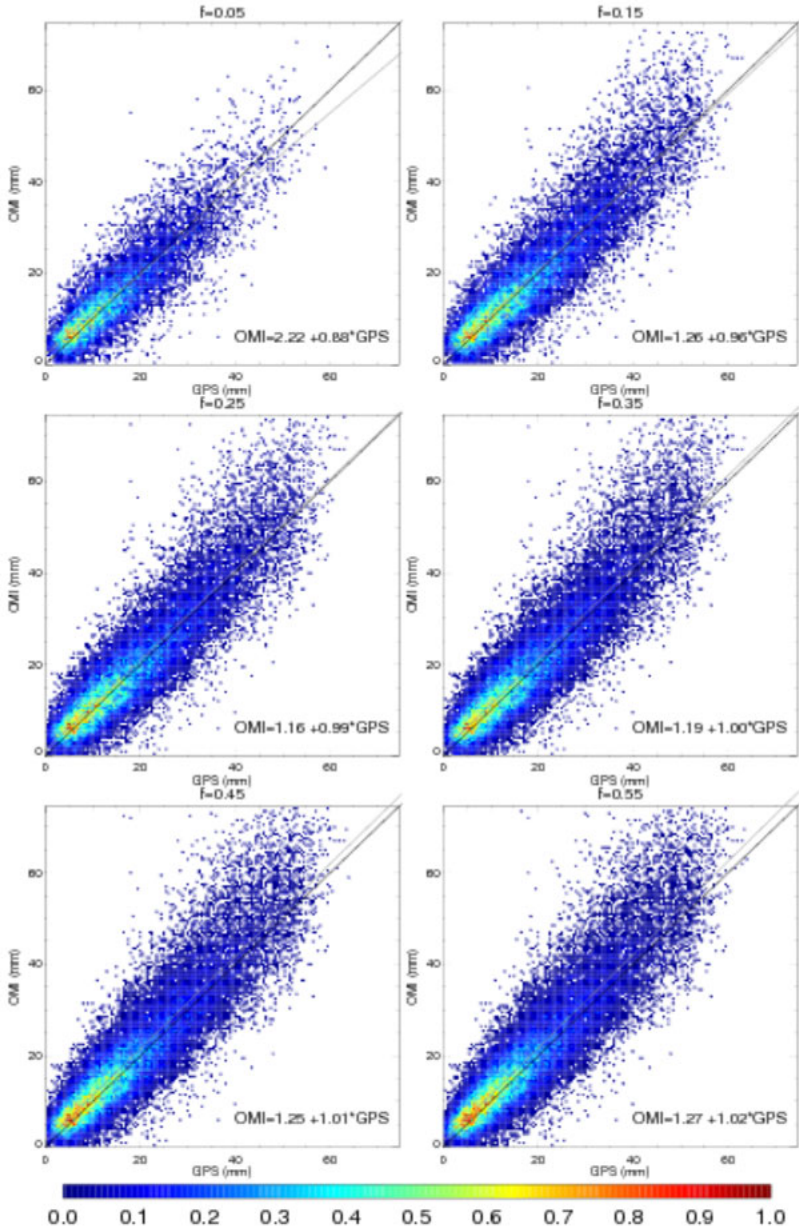
278 In addition, as shown by the GPS versus OMI joint distributions for different cloud fraction
279 thresholds in Figure 4, the $f \geq 0.15$ cases have larger effective dynamical ranges which tend to
280 favor better correlations. For example, there is a larger fraction of data pairs with TCWV > 30
281 mm for $f = 0.15$ than for $f = 0.05$. The regression line for $f = 0.15$ ($\text{OMI} = 1.26 + 0.96 * \text{GPS}$)
282 shows an apparent improvement over that for $f = 0.05$ ($\text{OMI} = 2.22 + 0.88 * \text{GPS}$). The best
283 regression line is arguably that for $f = 0.25$ ($\text{OMI} = 1.16 + 0.99 * \text{GPS}$) or $f = 0.35$ ($\text{OMI} = 1.19 +$
284 $1.00 * \text{GPS}$), though the mean bias and scatter are larger than those for $f < 0.25$ (Figure 4).

285 In brief, $f = 0.05$ leads to the lowest overall bias and scatter of the co-located data; $f = 0.15$
286 doubles the number of co-located data pairs and leads to the largest improvement in the
287 correlation coefficient; $f = 0.25$ (or 0.35) leads to the best linear regression line; the bias and
288 standard deviation increase with cloud fraction threshold. Hence, cloud fraction thresholds in the
289 range of $f = 0.05 - 0.25$ seems reasonable for filtering OMI TCWV, depending on applications.



290

291 **Figure 3.** Dependence of various parameters on the cloud fraction threshold (f) used for filtering
 292 OMI data. Other filtering criteria remain the same as those for Figure 2. The parameters are (a)
 293 number of co-located OMI and GPS data pairs; (b) linear correlation coefficient between OMI
 294 and GPS TCWV; (c) mean of OMI-GPS in mm; (d) standard deviation of OMI-GPS in mm.
 295 Results are derived from the co-located Version 4.0 OMI and GPS data for the whole year of
 296 2006.

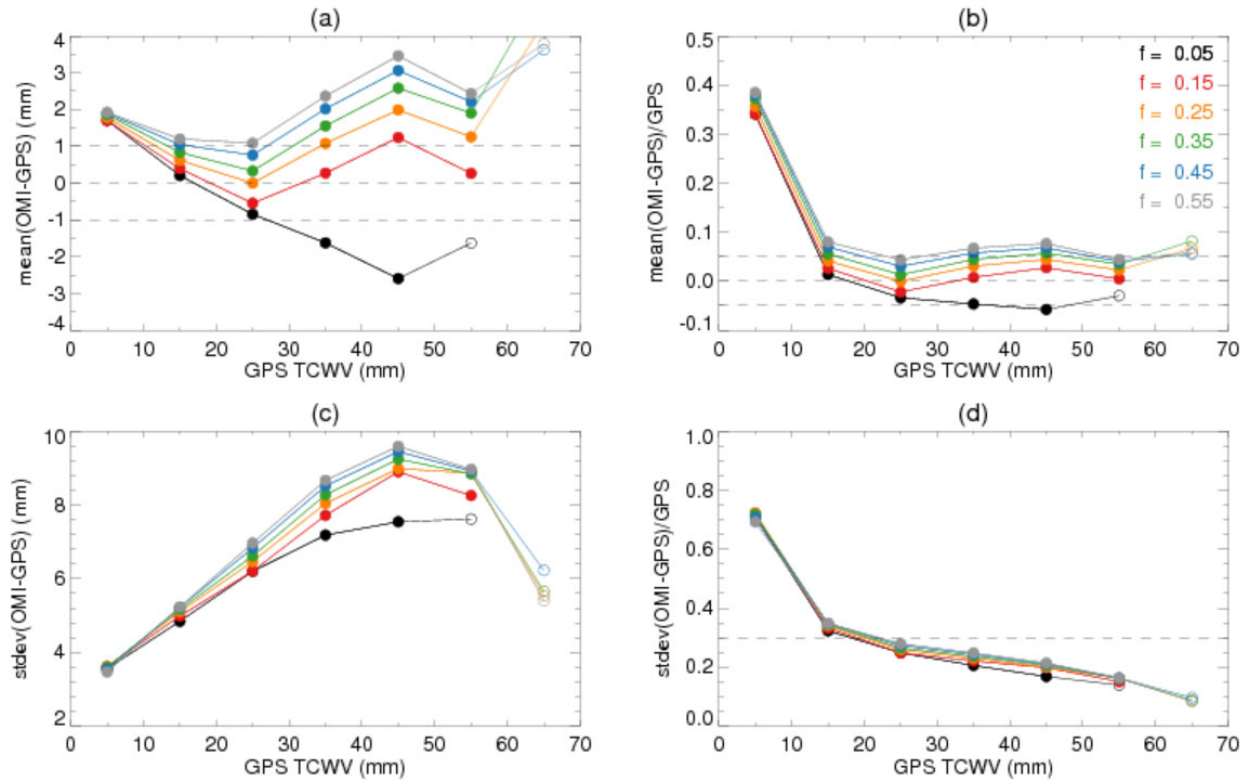


297

298 Figure 4. Normalized joint distributions of GPS versus Version 4.0 OMI TCWV for different
 299 cloud fraction thresholds. Results are derived from the co-located data pairs for 2006. [The OMI](#)
 300 [data filtering criteria](#) are the same as those for Figure 3. In each panel, the 1:1 line is plotted in
 301 [black](#), the linear regression line is plotted in gray and indicated by the formula in the lower right
 302 [corner](#).

303 To further characterize the effect of cloud fraction threshold on the comparison [between GPS](#)
 304 [and OMI](#), in Figure 5, we examine the mean and standard deviation (σ) of OMI-GPS for each 10
 305 mm GPS TCWV bin. The results are derived from the same sets of co-located GPS and OMI

306 data as those used in Figure 3 and Figure 4. The filled symbols are for the cases where the
 307 number of GPS and OMI data pairs within the corresponding TCWV bin is > 1% of the total
 308 number of data pairs, and the open symbols are for < 1%. As the filled symbols represent better
 309 statistics, we will focus on them below.



310

311 **Figure 5. Parameters** for each 10 mm TCWV bin. Curves with different colors are for different
 312 cloud fraction thresholds (f) as indicated in Panel (b). The OMI filtering criteria remain the same
 313 as those for Figure 3 and 4. Symbols are filled if the fraction of data pairs within the TCWV
 314 interval is > 1% of all the available data pairs, and are open otherwise. The parameters are (a)
 315 mean of OMI-GPS in mm, (b) relative bias defined as $(\text{OMI-GPS})/\text{GPS}$, (c) standard deviation
 316 (σ) of OMI-GPS in mm, and (d) relative scatter defined as σ/GPS . Results are for all days in
 317 2006. Dashed lines are meant to facilitate visualization.

318

319 Figure 5(a) shows that the means of OMI-GPS vary between ± 4 mm following “V”-shaped
 320 curves whose minima occur in the TCWV = 20 – 30 mm bin except for $f = 0.05$. The curves shift
 321 upward with increasing cloud fraction thresholds, suggesting that OMI cloudy-sky TCWV is
 322 generally larger than OMI clear-sky TCWV. Other things being equal, cloud formation indicates

323 water vapor saturation and therefore a larger amount of TCWV than that under clear-sky
324 condition. The smallest absolute bias for $10 < \text{TCWV} < 20$ mm occurs at $f = 0.05$, that for $20 <$
325 $\text{TCWV} < 30$ mm occurs at $f = 0.25$, and that for $30 < \text{TCWV} < 40$ mm occurs at $f = 0.15$. The $f =$
326 0.15 and $f = 0.25$ curves show the best overall performance according to Figure 5(a) as they are
327 within 1 mm of zero for $10 < \text{TCWV} < 40$ mm, while other curves come within 1 mm of zero in
328 narrower TCWV ranges. Figure 5(b) shows the relative bias which is defined as the mean of
329 $(\text{OMI-GPS})/\text{GPS}$. The relative biases decrease sharply from $\sim 40\%$ to $\sim 5\%$ as GPS TCWV
330 increases from the $\text{TCWV} = 0 - 10$ mm bin to the $\text{TCWV} = 10 - 20$ mm bin, and generally stay
331 less than $\sim 5 - 10\%$ for larger TCWV values. Figure 5(c) shows that σ increases from ~ 3.5 mm
332 for $\text{TCWV} = 0 - 10$ mm to ~ 9.5 mm for $\text{TCWV} = 40 - 50$ mm (the percentage of data with
333 $\text{TCWV} > 50$ mm is very small). In most cases, larger cloud fraction thresholds correspond to
334 larger σ values. This is consistent with the larger dynamical range (due to a larger fraction of
335 data with high TCWV) for larger cloud fraction threshold (Figure 4). In fact, the relative scatter,
336 defined as the mean of σ/TCWV , shows little difference among the f values (Figure 5d). The
337 relative scatter decreases with TCWV, with the sharpest decrease from ~ 0.7 to ~ 0.3 between
338 $\text{TCWV} = 0 - 10$ mm and $\text{TCWV} = 10 - 20$ mm (Figure 5d).

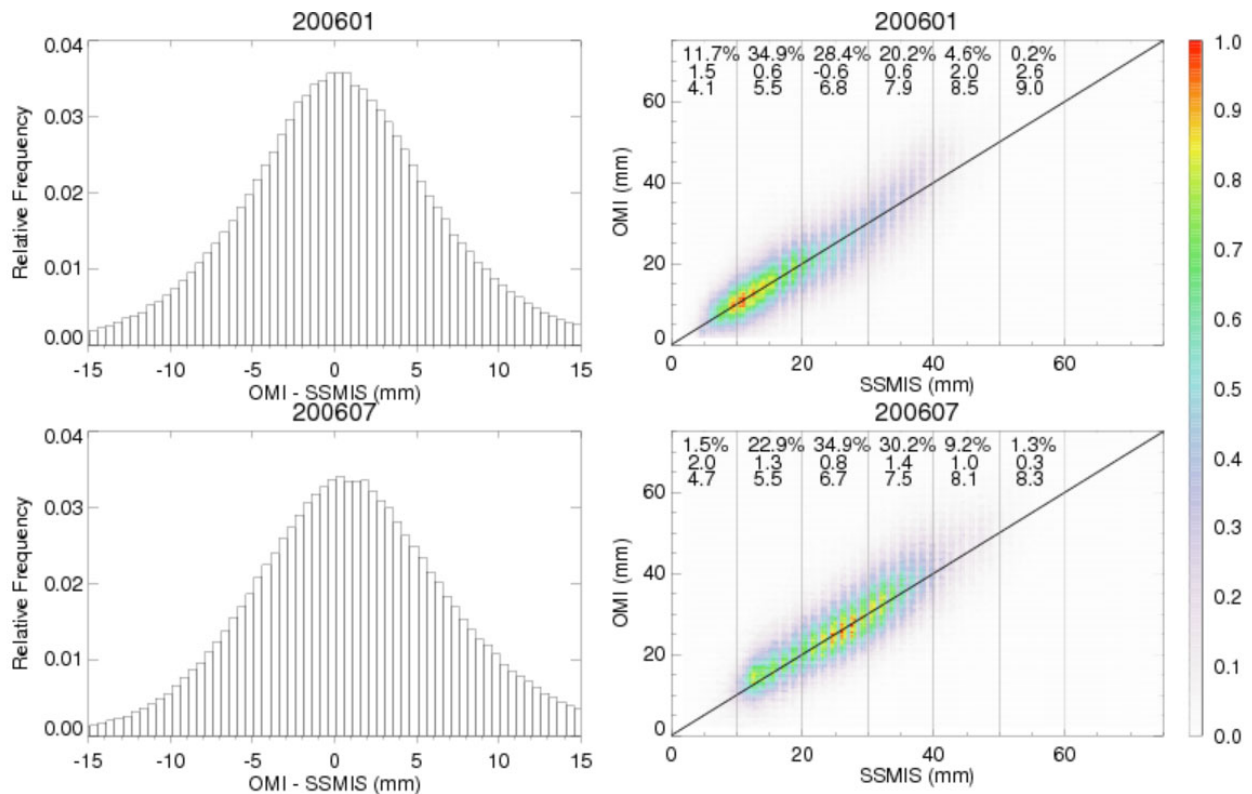
339 ___ In short, Version 4.0 OMI agrees with GPS within 1 mm for $10 < \text{TCWV} < 40$ mm when $f =$
340 0.15 and $f = 0.25$ are used; when $f = 0.05$ is used, the bias and scatter are the smallest for
341 $10 < \text{TCWV} < 20$ mm; but, for $\text{TCWV} < 10$ mm, OMI TCWV is too high and has large relative
342 scatter. The latter is expected from the low signal-to-noise ratio when $\text{TCWV} < 10$ mm in the
343 OMI retrieval.

344 **3.2 OMI and SSMIS over ocean**

345 To evaluate Version 4.0 OMI TCWV over the oceans, we compare against the microwave
346 TCWV data from SSMIS on board the Defense Meteorological Satellite Program (DMSP)'s F16
347 satellite. The SSMIS data are derived by Remote Sensing Systems (RSS) using their Version 7
348 algorithm (www.remss.com) and have a retrieval accuracy of better than 1 mm (Wentz, 1997;
349 Mears et al., 2015). For clear-sky comparison, we use the daily $0.25^\circ \times 0.25^\circ$ SSMIS data for
350 January and July 2006 and filter out the pixels affected by rain and cloud liquid water. Diedrich
351 et al. (2016) found that the diurnal cycle in TCWV is generally within 1% to 5% of the daily
352 mean, with a minimum between 0600 LT and 1000 LT and a maximum between 1600 LT and

353 2000 LT, though larger diurnal cycle exist for special cases. To reduce the influence of diurnal
 354 cycle, we average the SSMIS data for the ascending and descending orbits of F16 (~2000 LT and
 355 0800 LT in 2006).

356 We generate daily $0.25^{\circ} \times 0.25^{\circ}$ Level 3 OMI TCWV from the de-striped Level 2 OMI
 357 swaths, with the requirement that MDQFL = 0, fitting RMS < 0.001, $0 < \text{TCWV} < 75$ mm, cloud
 358 fraction < 0.05, and cloud top pressure > 750 mb. There are typically 15 Level 2 swaths per day.
 359 The gridding program uses a tessellation method that weighs the contribution of a Level 2 data
 360 point by its area within the Level 3 grid square and its spectrum fitting uncertainty (Wang et al.,
 361 2014, 2016). The filtered daily Level 3 SSMIS and OMI data are compared for each month. We
 362 find 548,223 and 847,678 co-located data pairs for January and July 2006, respectively.



363

364 **Figure 6.** Comparisons between Version 4.0 OMI and SSMIS over the oceans for (top) January
 365 2006 and (bottom) July 2006. Panels in the left column show the relative occurrence frequency
 366 of OMI-SSMIS (mm). Panels in the right column show the normalized joint distribution of
 367 SSMIS versus OMI TCWV (mm).

368

369 The left column of Figure 6 shows the distribution of OMI-SSMIS for January and July
370 2006. For July, the mean of OMI-SSMIS is 1.1 mm with a standard deviation of 6.8 mm, the
371 mean absolute error |OMI-SSMIS| is 5.2 mm; for January, the mean error, standard deviation and
372 mean absolute error are 0.4 mm, 6.5 mm and 5.0 mm, respectively. This suggests a slightly better
373 agreement for January than for July. In comparison with the (OMI-GPS) over land (Section 3.1),
374 OMI-SSMIS over the oceans has somewhat larger bias and standard deviation. However, as
375 TCWV over the oceans are generally larger than that over land (compare Figure 6 with Figure
376 2), the relative bias and scatter are actually similar.

377 The right column of Figure 6 shows the normalized joint distribution of SSMIS versus OMI
378 for January and July 2006. The correlation coefficients are $r = 0.84$ and 0.82 for January and
379 July, respectively. For January, OMI-SSMIS remains within 0.6 mm of zero for TCWV in the 10
380 – 40 mm range, but is 1.5 mm for TCWV in the 0 – 10 mm range (only a small fraction of data
381 pairs have TCWV > 40 mm); for July, OMI-GPS is 0.8 mm for the TCWV = 20 – 30 mm bin,
382 and varies between 0.8 and 1.4 mm for TCWV in the 10 – 50 mm range (only a small fraction of
383 data pairs have TCWV < 10 mm or > 50 mm). For TCWV bins that have > 5% of the data pairs,
384 the standard deviation of OMI-SSMIS vary between 4.1 and 8.1 mm. Overall, Version 4.0 OMI
385 data compare reasonably well with SSMIS data for TCWV in the 10 – 40 mm range, with the
386 smallest bias occurring in the TCWV = 20 – 30 mm bin.

387 The agreement between Version 4.0 OMI with SSMIS is better than that between Version 3.0
388 OMI and SSMIS. For July 2007, using the same data filtering criteria as before, we find that
389 Version 3.0 OMI – SSMIS has a mean of 3.2 mm with a standard deviation of 7.8 mm. The bias
390 is much larger than that for Version 4.0 OMI – SSMIS. Again, this is because of the much larger
391 SCD of Version 3.0 OMI TCWV due to the water vapor reference spectrum (Supplementary
392 Figure 1).

393 Table 3 shows the effect of cloud fraction threshold (f) on the comparison between SSMIS
394 and Version 4.0 OMI TCWV. The comparisons are performed using daily filtered Level 3 data
395 for July 2006. For SSMIS, we filter out pixels affected by rain. This is less restrictive than that
396 used for Figure 6 as pixels with cloud liquid water are kept here. For OMI, we require MDQFL =
397 0, $RMS < 0.001$, $0 < TCWV < 75$ mm, cloud top pressure > 750 mb and cloud fraction < f .
398 Results show that OMI is higher than SSMIS by 0.02 – 3.07 mm for $f = 0.05 – 0.45$. **The**

399 difference between the $f = 0.05$ case of Table 3 and the $f = 0.05$ case of Figure 6 is due to the
 400 relaxed SSMIS filtering criteria. The closest agreement in terms of the mean and standard
 401 deviation of OMI-SSMIS occurs when $f = 0.05$. The number of SSMIS and OMI data pairs more
 402 than doubles between $f = 0.05$ and $f = 0.15$. The linear correlation coefficient varies between
 403 0.82 and 0.85 within the range of f values considered. The best linear regression line (OMI =
 404 $0.70 + 1.02 * \text{SSMIS}$) occurs when $f = 0.15$. Therefore, for OMI over the oceans, we recommend
 405 using cloud fraction threshold $f = 0.05 - 0.15$, in combination with the other usual data filtering
 406 criteria, though users are advised to make their own decisions based on their tolerance and
 407 applications.

408 **Table 3.** Effect of cloud fraction threshold on the comparison between SSMIS and Version 4.0
 409 OMI TCWV for July 2006. f : OMI cloud fraction threshold; N: number of qualifying data pairs;
 410 P: Percentage of qualifying data pairs with respect to the total number of qualifying SSMIS data
 411 points; Mean: mean of OMI-SSMIS in mm; σ : standard deviation of OMI-SSMIS in mm; MAE:
 412 Mean absolute error $|\text{OMI-SSMIS}|$ in mm; r : correlation coefficient between SSMIS and OMI;
 413 R^2 : coefficient of determination for linear regression $\text{OMI} = b + k * \text{SSMIS}$, where OMI and
 414 SSMIS are in mm; b : Intercept of linear regression; k : slope of linear regression.

f	N	P (%)	Mean	σ	MAE	r	R^2	b	k
0.05	1,048,879	7.4	0.02	7.11	5.39	0.82	0.67	1.43	0.95
0.15	2,837,032	20.0	1.38	7.82	5.84	0.84	0.71	0.70	1.02
0.25	3,932,468	27.8	2.20	8.09	6.09	0.84	0.71	1.11	1.04
0.35	4,819,185	34.0	2.73	8.22	6.24	0.85	0.72	1.45	1.05
0.45	5,537,003	39.1	3.07	8.26	6.32	0.85	0.72	1.62	1.06

415
 416 Lowering the value for cloud top pressure threshold also leads to larger bias and scatter. For
 417 example, when cloud fraction threshold $f = 0.05$ and cloud top pressure > 500 mb are used, the
 418 mean and standard deviation of OMI-SSMIS become 0.80 mm and 7.9 mm, both are larger than
 419 those for $f = 0.05$ in Table 3, though the linear regression line improves to $\text{OMI} = 0.63 + 1.01 * \text{SSMIS}$
 420 RSS due to an increase in the dynamical range of TCWV. It should be noted that the OMCLDO2
 421 cloud product shows good agreement with ground-based observations for clouds at altitudes
 422 lower than 2.5 km where single cloud layers dominate, but shows significant bias and large
 423 scatter for clouds at altitudes higher than 2.5 km where multi-layer clouds dominate (Veeffkind et

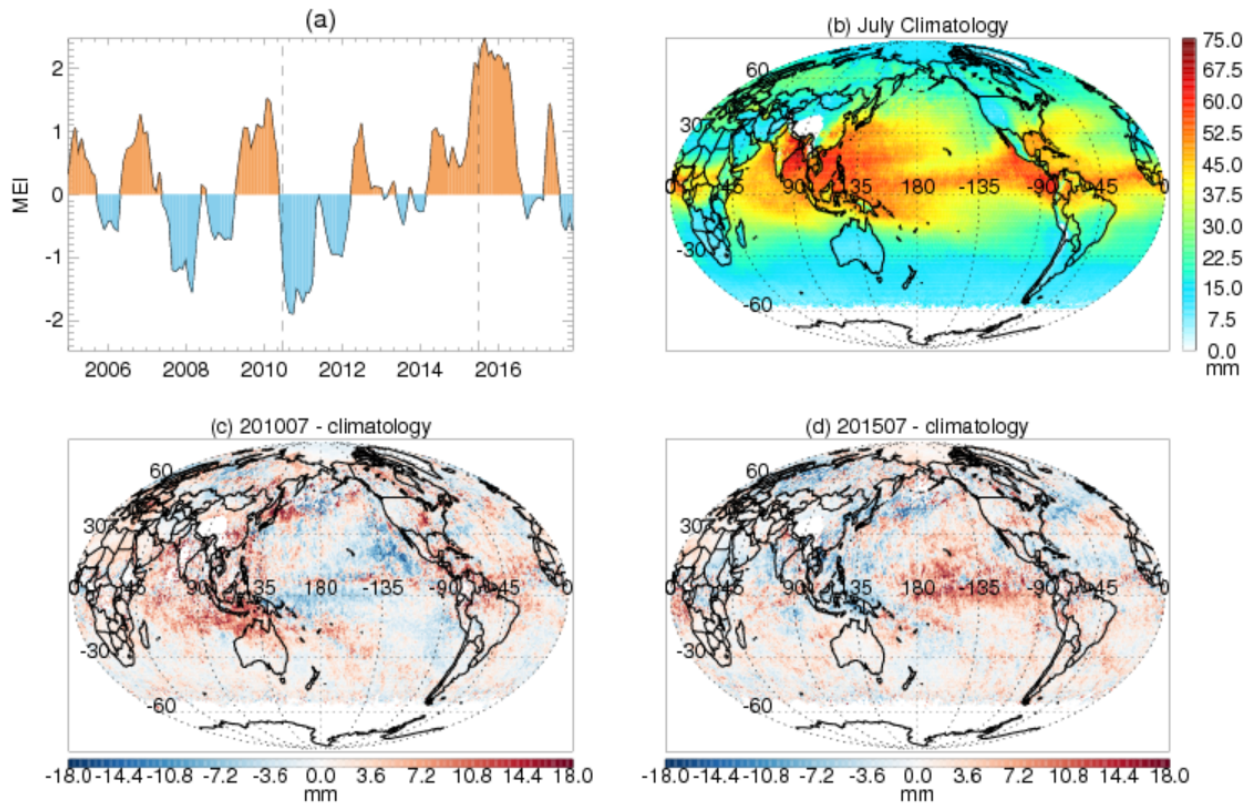
424 [al., 2016](#)). Thus, OMI TCWV data corresponding to low cloud top pressure ([high altitude](#))
425 [should be used with caution](#). Relaxing the filtering criteria for both cloud fraction and cloud top
426 pressure will lead to larger bias and scatter, therefore, it is not recommended. As an example, for
427 cloud fraction < 0.15 and cloud top pressure > 300 mb, the mean (standard deviation) of OMI-
428 SSMIS becomes 2.8 mm (9.0 mm) for July 2006.

429 **4 Application**

430 **4.1 El Niño / La Niña**

431 In Figure 7, we examine the signals associated with El Niño and La Niña in Version 4.0 OMI
432 TCWV. Panel (a) shows the Multivariate ENSO Index (MEI) from NOAA (Wolter and Timlin,
433 1998) (<https://www.esrl.noaa.gov/psd/enso/mei/>). Positive (negative) values correspond to El
434 Niño (La Niña) conditions. We examine the [anomalies](#) in TCWV for July 2010 (MEI = -1.103,
435 La Niña) and July 2015 (MEI = 1.981, El Niño) in the bottom row. Although these events are
436 strong within the OMI record (from 2005 to the present), they are mild in comparison with the
437 extrema. Between 1950 and 2018, the maximum MEI is 3.008 (in March 1983) and the
438 minimum MEI is -2.247 (in June 1955).

439



440

441 **Figure 7.** Top row: (a) Multivariate ENSO Index. Dashed vertical lines indicate July 2010 and
 442 July 2015; (b) TCWV (mm) climatology for July derived from Version 4.0 OMI data. Bottom
 443 row: TCWV anomaly (mm) with respect to the climatology for (c) July 2010 and (d) July 2015.

444

445 To examine the changes in OMI TCWV under different conditions, we first generate the
 446 monthly Level 3 ($0.5^\circ \times 0.5^\circ$) OMI TCWV using the Level 2 data for July 2005 and July 2015
 447 using the method described in Section 3.2 (with a cloud fraction threshold of $f = 0.15$ and a cloud
 448 top pressure threshold of 750 mb). Then, using the same data filtering criteria, we derive the
 449 climatology for July using all the Level 2 July data between 2005 and 2015 (Figure 7b). Finally,
 450 we plot the deviations from the climatology (mm) for July 2010 and July 2015 in Figure 7(c) and
 451 7(d), respectively.

452 The TCWV anomalies exhibit large-scale patterns. The pattern for July 2015 largely opposes
 453 that for July 2010. Particularly, in July 2015 under El Niño conditions, TCWV are higher in the
 454 equatorial central and eastern Pacific and lower in the Indonesia region; while in July 2010 under
 455 La Niña conditions, TCWV are lower in the tropical eastern Pacific and equatorial western

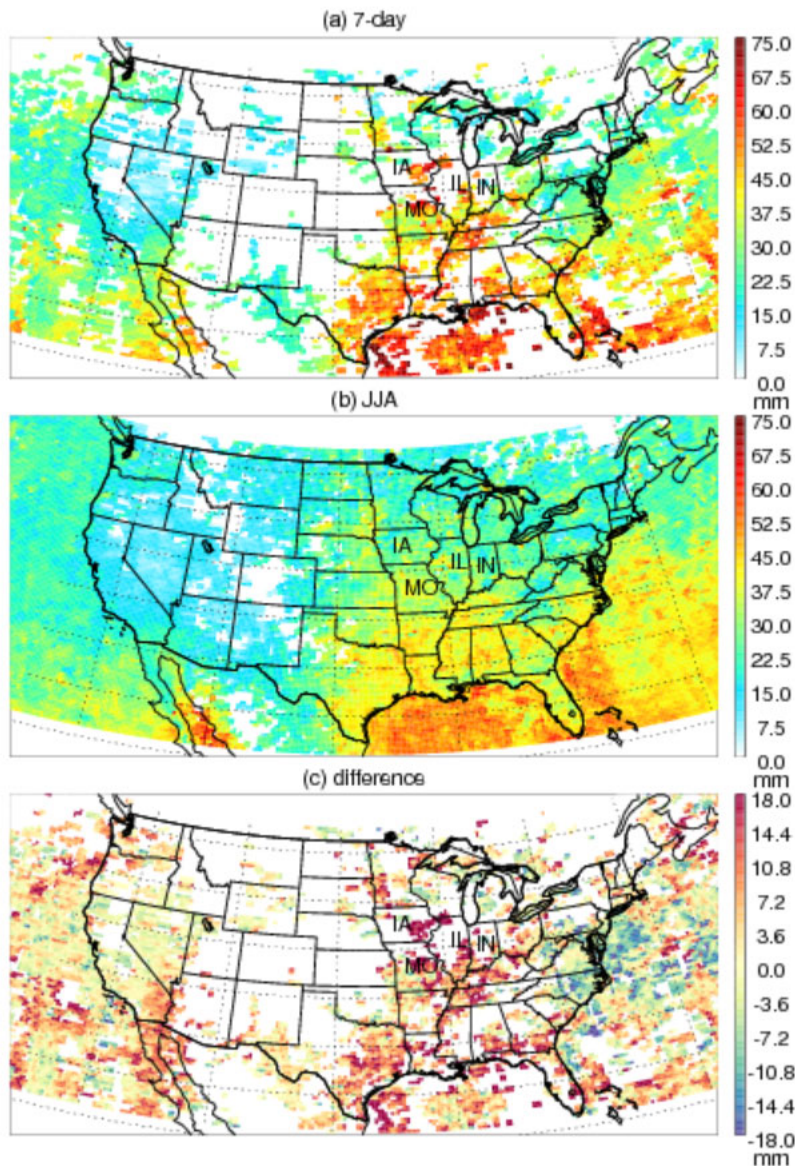
456 Pacific and higher in Indonesia and the Indian Ocean. The overall patterns largely conform to the
457 results derived from the Hamburg Ocean Atmosphere Parameters and Fluxes from Satellite Data
458 (HOAPS) data (Shi et al., 2018). ~~The HOAPS climatology is derived from a longer time series~~
459 ~~(1998-2014), which may be among the reasons for the differences in details between the results.~~

460 4.2 Corn Sweat

461 “Corn sweat” refers to a hot and humid condition associated with heat waves which results in
462 large evapotranspiration rate in the Midwestern United States where cropland is often the
463 dominant land usage type. Besides evaporation, transpiration by plants, such as corn, draws
464 water from the soil to the atmosphere, enhancing the humidity and increasing the heat index. A
465 corn sweat event from July 18 to July 24 in 2016 made news in the US. This event is examined
466 in Figure 8 using the Version 4.0 OMI TCWV.

467 Figure 8 (a) and 8(b) show the Level 3 ($0.25^{\circ} \times 0.25^{\circ}$) OMI TCWV for July 18 - July 24
468 (7-day) and June 1 – August 31 (JJA) in 2016, respectively. The 7-day period corresponds to the
469 corn sweat event. The $0.25^{\circ} \times 0.25^{\circ}$ Level 3 data are derived using the same filtering criteria as
470 those used for Figure 7. Figure 8(c) indicates the anomaly associated with the corn sweat event
471 relative to the JJA mean. High TCWV is observed for the 7-day period from the Gulf coast to the
472 Midwestern US. Besides the Gulf region, the largest TCWV enhancements (of up to 18+ mm)
473 occur in parts of Iowa (IA), Missouri (MO), Illinois (IL) and Indiana (IN). Elevated TCWV is
474 also observed by several GPS stations in the general area during the same time period, though
475 coincident OMI data are not found at the stations (Supplementary Figure 3). At a few stations,
476 high TCWV persisted a couple more days after July 24 which is most likely related to a change
477 in the weather. As shown by the surface pressure observations at the GPS stations, the Midwest
478 is under the control of a high-pressure system during the corn sweat period and a low-pressure
479 system afterwards (Supplementary Figure 4).

480

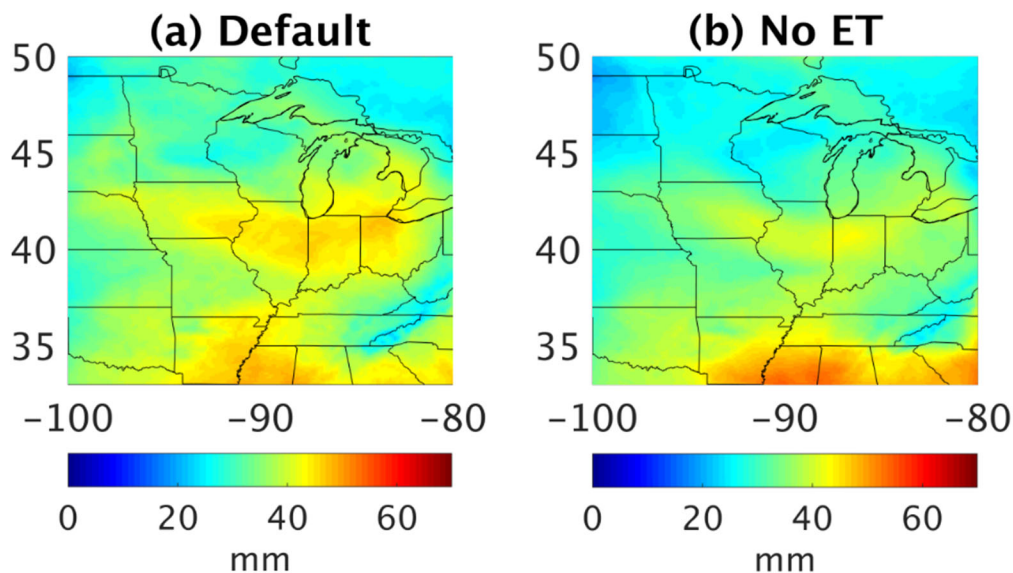


481
 482 **Figure 8.** Level 3 ($0.25^{\circ} \times 0.25^{\circ}$) OMI TCWV (mm) generated using the Level 2 data during (a)
 483 July 18 - July 24, 2016 and (b) June 1 - August 31, 2016. (c) The difference of (a) - (b) in mm.
 484 The abbreviations for the states most affected by the event are indicated in the map.

485
 486 To assess the significance of evapotranspiration for the Midwestern US during the corn sweat
 487 event, we carried out a sensitivity study using the Weather Research and Forecasting (WRF)
 488 model v3.9.1 (Skamarock et al., 2008). The model was run on a 36-km parent domain and a 12-
 489 km nested domain, covering the relevant areas of the US. The physics parameterizations

490 included the WRF Single-Moment (WSM) 6-Class Microphysics (Hong and Lim, 2006), the
491 Kain-Fritsch (KF) subgrid cumulus parameterization (Kain, 2004), the Yonsei University (YSU)
492 planetary boundary layer scheme (Hong et al., 2006), the Noah Land-Surface Model (Ek et al.,
493 2003; Chen and Dudhia, 2001), and the Rapid Radiative Transfer Model (RRTM). Horizontal
494 turbulent diffusion was based on the standard Smagorinsky first-order closure. The initial and
495 lateral boundary conditions were from the 3-hourly [NCEP North American Regional Reanalysis](#)
496 [\(NARR\)](#) at 32-km resolution. To reduce the uncertainty associated with lateral boundary
497 condition [for](#) the nested domain, we nudged the model in the parent domain toward the
498 reanalysis, but left the nested domain running freely.

499 To diagnose the contribution of evapotranspiration, the model was run from July 19th to July
500 22nd of 2016 with and without evapotranspiration (calculated in the Noah Land-Surface model).
501 The results for July 21st are shown in Figure 9. TCWV is generally lower in the [interior of the](#)
502 [domain for the run without evapotranspiration \(No ET\)](#). [The higher TCWV in the No ET run](#)
503 [near the southern boundary reflects non-linear water vapor transport from the Gulf region](#).
504 [Turning off evapotranspiration not only directly affects the water vapor flux from the surface but](#)
505 [also indirectly influences other meteorological variables, such as winds](#). [Thus, there is a](#)
506 [difference in the water vapor flux across the domain boundary](#). The difference between the
507 [default and No ET](#) runs in Figure 9 suggests that evapotranspiration contributes about 15 – 25%
508 of the TCWV in the Midwestern US during the corn sweat event. A detailed study incorporating
509 TCWV data with the WRF model will be carried out in future work.



510

511 **Figure 9.** WRF simulations of TCWV (mm) for Midwestern US on 07/21/2016 for the run (a)
512 with and (b) without evapotranspiration.

513

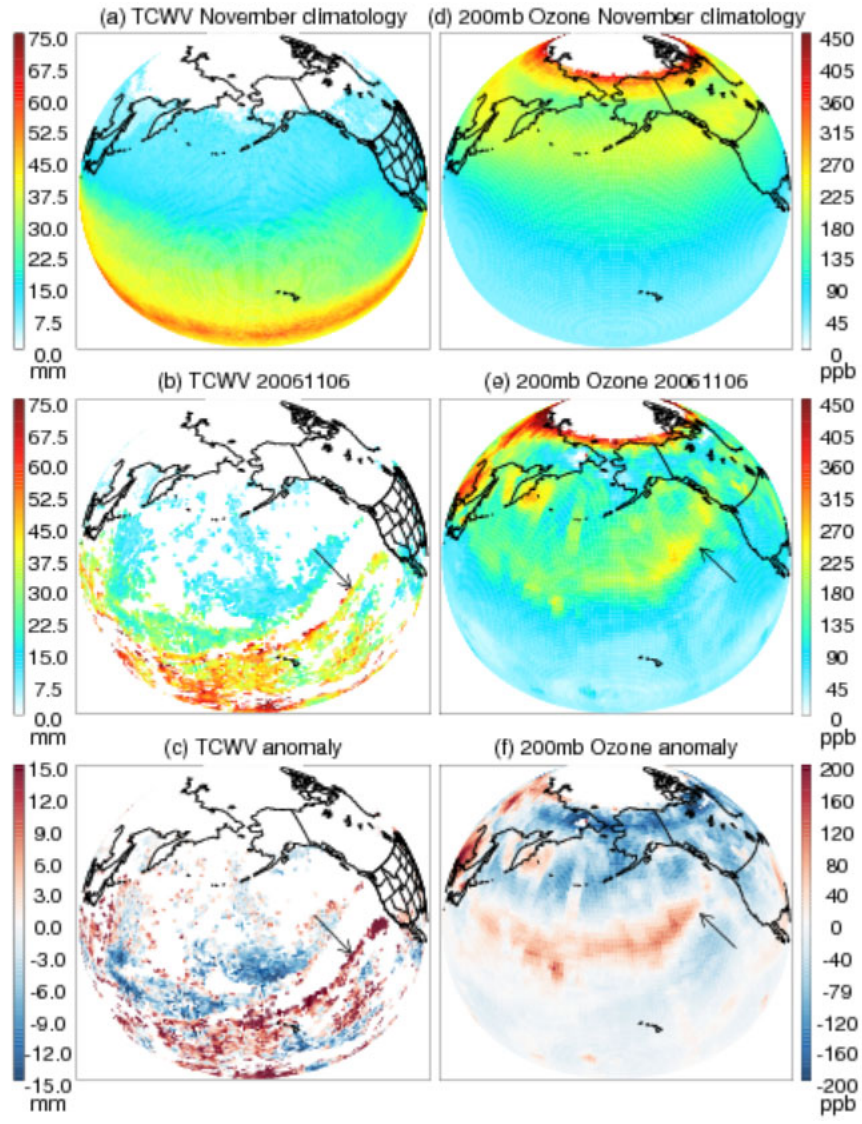
514 **4.3 Atmospheric River (AR)**

515 **4.3.1 An Intense AR in OMI data**

516 ARs are narrow elongated bands with high TCWV in the atmosphere. With flow rates similar
517 to those of large rivers, ARs are highly important in the global hydrological cycle (Zhu and
518 Newell, 1998). Land-falling ARs can lead to heavy orographic precipitation that affects areas
519 such as the west coast of North America and Europe (Gimeno et al., 2014; [Neiman et al., 2008b](#)).

520 The extreme AR of November 6th – 7th, 2006 brought devastating flood to the Pacific
521 Northwest – the region in western North America bounded by the Pacific to the west and the
522 Cascade mountain range to the east. This AR is described in detail in [Neiman et al., 2008a](#). The
523 signature of this AR is captured in the Version 4.0 OMI TCWV data. The left column of Figure
524 10 shows the Level 3 OMI TCWV and its anomaly on November 6th, 2006. The Level 3 data are
525 generated following the same procedure as that used for Figure 8. Although many pixels are
526 missing because of the cloud filtering (cloud top pressure > 750 mb, cloud fraction < 0.15) and
527 other criteria, the leading edge of the AR is noticeable as an elongated band of high TCWV (15+
528 mm above the climatology) extending from Hawaii to Northern California (indicated by arrows
529 in [Figure 7\(b\) and 7\(c\)](#)). The position of the AR in OMI TCWV agrees well with that in [Special
530 Sensor Microwave/Imager \(SSM/I\)](#) microwave observation (Neiman et al., 2008a).

531 The right column of Figure 10 shows the Level 3 OMI ozone mixing ratio interpolated to 200
532 mb and its anomaly. The OMI ozone data are retrieved using the SAO ozone profile algorithm
533 (Liu et al., 2010; Huang et al., 2017, 2018). The climatology is derived by averaging all monthly
534 Level 3 data for November from 2004 to 2017. The global distribution of ozone at 200 mb shows
535 low mixing ratio in the low latitudes and high mixing ratio in the high latitudes, opposite to the
536 global distribution of TCWV. The anomaly shows a curvilinear band [of high ozone](#) that is
537 parallel to the AR in the left column, but is located further to the west. This feature indicates
538 intrusion of ozone rich stratospheric air along the polar front, and is [associated with the same
539 extra-tropical cyclone as the AR is](#).



540

541 **Figure 10.** The Level 3 (top row) climatology, (middle row) data on November 6th, 2016 and
 542 (bottom row) anomaly on November 6th, 2016 with respect to the climatology for (left column)
 543 Version 4.0 OMI TCWV (mm, 0.5°×0.5°) and (right column) OMI ozone mixing ratio (ppb,
 544 1°×1°) interpolated to 200 mb.

545

546 **4.3.2 OMI Data Assimilation for the AR**

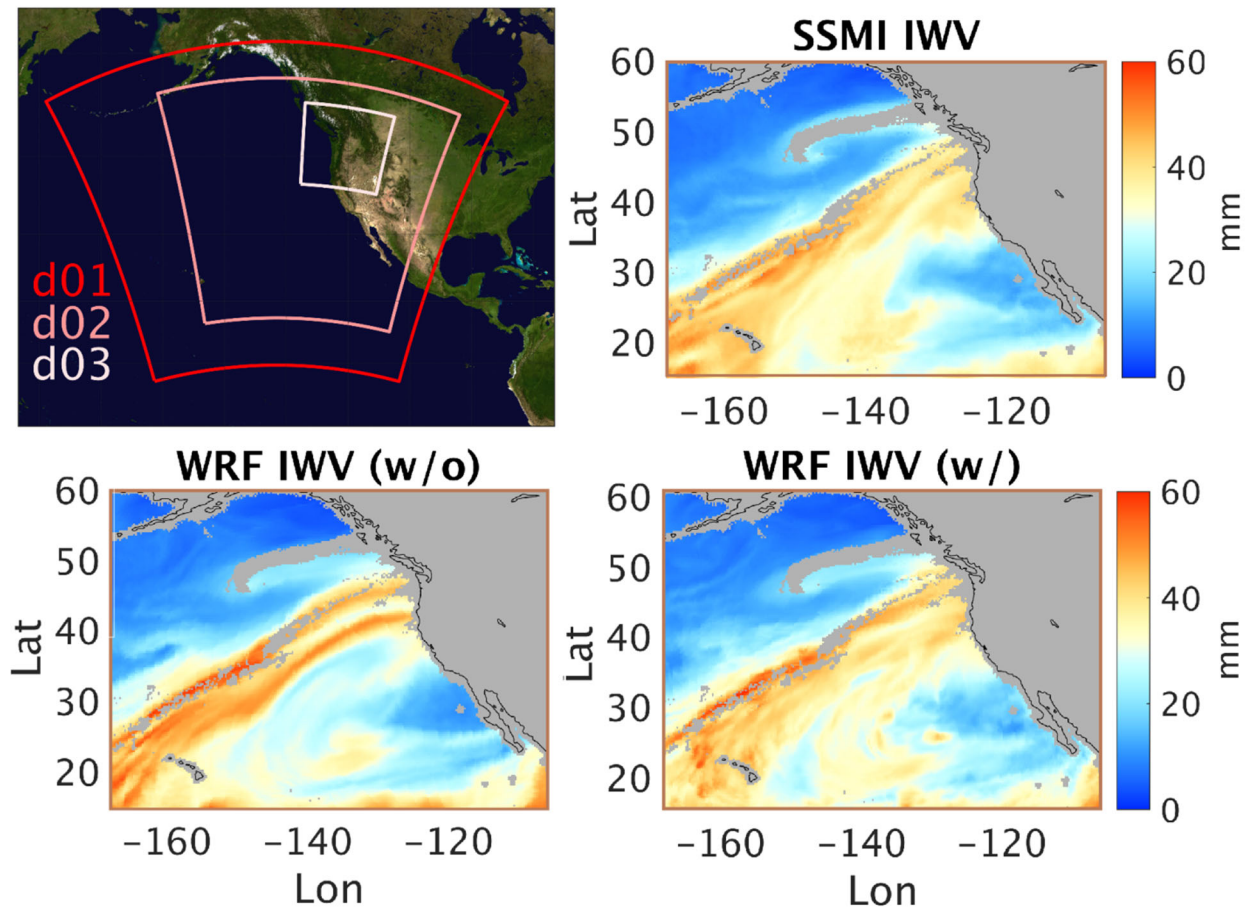
547 To evaluate the potential of OMI water vapor data to improve numerical weather forecasts,
 548 we conducted a data assimilation experiment from November 2nd to November 8th of 2016 using
 549 WRF v3.9.1 and Version 4.0 OMI TCWV. The model was configured with a 27-km (290×270

550 surface grid points with 51 vertical levels), a 9-km (586×586×51 points) and a 3-km
 551 (541×526×51) nested domains in a Lambert projection over the relevant portion of the Pacific
 552 and North America (Figure 11 top left). The domains are designed for the November 6 AR event
 553 and its associated precipitation at landfall. The model has the same physics parameterizations as
 554 those used in Section 4.2 except that a more sophisticated double-moment microphysics scheme
 555 is used in the 3-km nest for quantifying precipitation. The initial and boundary conditions for the
 556 27-km domain were from the 1°×1° NCEP FNL reanalysis. One-way nesting is used for the
 557 inner domains. To evaluate the model’s skill at simulating the AR and the contribution of OMI
 558 TCWV to the quality of the simulation, we did not nudge the run towards the reanalysis, nor
 559 assimilate the observed sea surface temperature within the computational domains.

560 The OMI TCWV is assimilated into the model using analytical optimal estimation (Rodgers,
 561 2000). This method minimizes the cost function $J(\mathbf{x}) = (\mathbf{y} - H\mathbf{x})^T \mathbf{E}^{-1}(\mathbf{y} - H\mathbf{x}) +$
 562 $(\mathbf{x} - \mathbf{x}^b)^T \mathbf{B}^{-1}(\mathbf{x} - \mathbf{x}^b)$, where x is the true TCWV, x^b is the a priori TCWV (from the model), y
 563 is the observed TCWV, H represents the model Jacobian, \mathbf{B} and \mathbf{E} are the error covariance
 564 matrices of the a priori and observation. \mathbf{B} is estimated using the 12-hour and 24-hour forecasts
 565 using the National Meteorological Center method (Parrish and Derber, 1992). \mathbf{E} is based on the
 566 fitting uncertainties of OMI data.

567 The a posteriori analysis ($\hat{\mathbf{x}}$) can be obtained from $\hat{\mathbf{x}} = \mathbf{x}^b + \mathbf{K}(\mathbf{y} - H\mathbf{x})$, where $\mathbf{K} =$
 568 $\mathbf{B}H^T(\mathbf{H}\mathbf{B}H^T + W^{-1}\mathbf{E})^{-1}$ is the Kalman gain, $W = \frac{(R^2 - r^2)}{(R^2 + r^2)}$ is the Cressman function to weigh the
 569 observations based on their Euclidian distance r to the model grids, and R is the influence radius
 570 of the observations. We simply assume R to be 1°, 0.5° and 0.25° for the 27-km, 9-km and 3-km
 571 domain to get a quick look at the results in this paper and leave a more vigorous quantification of
 572 R to future work.- The a posteriori TCWV is solved hourly when OMI data are available and is
 573 used to initialize the next simulation window.

574 During the assimilation, we adjust the OMI data using the AMF calculated with the modeled
 575 water vapor profile ($OMI_{satellite}^{adjusted} = \frac{OMI_{satellite} \times AMF_{satellite}}{AMF_{model}}$) and the scattering weights provided
 576 with the Level 2 OMI data. This can reduce the observational error associated with using the
 577 monthly mean water vapor profile in the operational OMI product. The standard deviation of the
 578 difference between $AMF_{satellite}$ and AMF_{model} is about 20%.



579

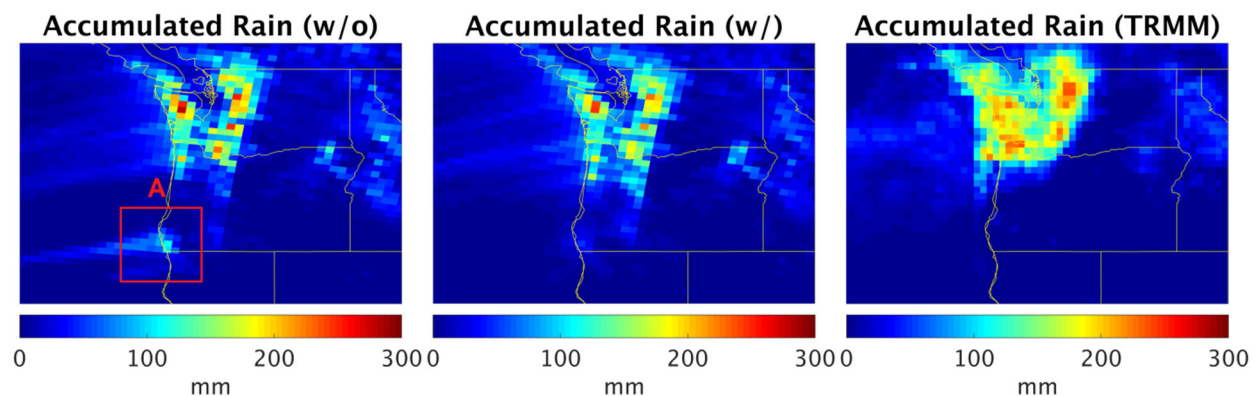
580 **Figure 11.** Top left: WRF model domain configuration for the November 2016 AR event. Top
 581 right: TCWV observed by SSM/I on November 6th, 2016. Bottom row: TCWV simulated by
 582 WRF on November 6th, 2016 (left) without and (right) with OMI data assimilation. Gray color
 583 indicates area with no SSM/I data.

584

585 Figure 11 shows the zoomed-in views of the AR on November 6th, 2016. The TCWV
 586 independently observed by SSM/I is shown in the upper right panel. The lower left and lower
 587 right panels show the model results without and with OMI TCWV assimilation. The model
 588 without assimilation shows an AR that is split into two parallel filaments making landfall at
 589 separate locations on the west coast of North America, where the TCWV is too high compared to
 590 the SSM/I observation, especially for the southern filament. As discussed later, this has a
 591 significant impact on precipitation (Figure 12). After assimilating OMI TCWV, the modeled

592 TCWV agrees much better with the SSM/I observation. The [spurious southern filament](#)
593 [disappeared, the](#) overall shape and magnitude of the AR are significantly improved.

594 The location and intensity of precipitation over land are crucial for local flood control and
595 water management, and are closely related to the shape and strength of AR at landfall. The 24-
596 hour accumulated precipitation on November 6 in the 3-km domain is examined in Figure 12.
597 The model output is [coarsened](#) to $0.25^\circ \times 0.25^\circ$ to match the resolution of the Tropical Rainfall
598 Measuring Mission ([TRMM](#)) observation product. The model without OMI data assimilation
599 produces spurious rainfall over the Oregon - California border (box A) as a result of the
600 [erroneously strong southern filament of the simulated AR](#) (Figure 11, lower left panel). This
601 artifact was removed after OMI data assimilation, showing better agreement with the
602 corresponding TRMM rainfall observation. [The difference in rainfall between the assimilation](#)
603 [and observation in the Oregon / Washington area is probably related to both the model error and](#)
604 [the data error, as well as the data density and distribution. A detailed error attribution for](#)
605 [precipitation is beyond the scope of this paper.](#)



606
607 **Figure 12.** The simulated rainfall accumulated from 0000 UTC to 2300 UTC (in mm) on
608 November 6, 2006 for the model (left) without and (middle) with OMI TCWV assimilation. The
609 rightmost panel show the accumulated rainfall observed by TRMM for the same time period.
610 Note that the 3-km model result is coarsened to match the resolution of the TRMM product.
611 Box A highlights the erroneously simulated precipitation in the run without OMI data
612 assimilation.

613

614 5 Summary and Conclusion

615 The Version 4.0 retrieval algorithm for OMI Total Column Water Vapor (TCWV) is presented
616 in this paper. The algorithm follows the usual two-step approach where Slant Column Density
617 (SCD) is derived from spectral fitting and Vertical Column Density (VCD) is obtained through
618 the ratio of SCD and Air Mass Factor (AMF). In Version 4.0, the spectral fitting no longer
619 considers common mode. The retrieval window (432.0 - 466.5 nm) results from a systematic
620 optimization that reflects trade-offs among several factors, including small fitting RMS, small
621 fitting uncertainty, large fraction of successful retrieval and long retrieval window length. The
622 AMF calculation uses the latest OMI O₂-O₂ cloud product (Veefkind et al., 2016) and monthly
623 variable vertical profiles from the MERRA-2 reanalysis (Gelaro et al., 2017).

624 The Version 4.0 OMI TCWV product is compared against the GPS network data over land
625 and the SSMIS microwave observations over the oceans for 2006. Version 4.0 OMI TCWV has
626 much smaller bias than Version 3.0 and has replaced previous versions on the Aura Validation
627 Data Center website. Version 4.0 OMI TCWV is characterized under different cloud conditions.
628 Under “clear-sky” condition (cloud fraction < 5% and cloud top pressure > 750 mb), the overall
629 mean of OMI-GPS over land is 0.32 mm with a standard deviation of 5.2 mm, and the smallest
630 bias occurs when TCWV is between 10 mm and 20 mm; the overall mean of OMI-SSMIS over
631 the oceans is 0.4 – 1.1 mm with a standard deviation of 6.5 - 6.8 mm, and the smallest bias
632 occurs for TCWV between 20 mm and 30 mm. The correlation coefficient between OMI TCWV
633 and the reference datasets realizes the largest gain when the cloud fraction threshold is increased
634 from 5% to 15%. The regression line appears the best when $f = 0.25$ is used over land and when f
635 = 0.15 is used over the oceans. But, larger cloud fraction leads to larger bias and scatter. Thus,
636 for most applications, we recommend to consider only OMI data with cloud fraction < 5% to
637 25% and cloud top pressure > 750 mb, in addition to main data quality flag = 0, no row anomaly,
638 fitting RMS < 0.001 and 0 < TCWV < 75 mm. Relaxing the cloud top pressure threshold has a
639 similar effect as relaxing the cloud fraction threshold. TCWV corresponding to low cloud top
640 pressure (high altitude) should be used with caution due to the degraded accuracy for these
641 clouds in the OMCLDO2 product.

642 As example applications of the Version 4.0 OMI TCWV data across a variety of temporal
643 and spatial scales, this paper examines the climate pattern associated with El Niño / La Niña, the
644 enhanced humidity during a week-long corn sweat event in the Midwest US, and the linear band
645 of high TCWV associated with an intense atmospheric river which made landfall on the west

646 coast of North America. Strong signals are found in OMI TCWV for all three examples. A data
647 assimilation experiment shows that the OMI TCWV data can help improve WRF's skill of
648 simulating the shape and intensity of the AR, as well as the accumulated rainfall near the coast.

649 Further improvement of the product can proceed from both spectral fitting and AMF
650 calculation, such as, water vapor reference spectrum, instrument slit-function and solar irradiance
651 for spectral fitting, aerosol correction and surface bi-directional reflectance for AMF calculation.

652

653 **Data availability**

654 The GPS network data are downloaded from NCAR (rda.ucar.edu/datasets/ds721.1). The SSMIS
655 data used in this paper are downloaded from the Remote Sensing Systems
656 (<http://www.remss.com/support/data-shortcut/>). The Multivariate ENSO Indices are downloaded
657 from NOAA (<https://www.esrl.noaa.gov/psd/enso/mei/table.html>). OMI TCWV and ozone
658 profile data are released through the Aura Validation Data Center (<https://avdc.gsfc.nasa.gov/>).

659

660 **Author contribution**

661 Huiqun Wang optimized the OMI TCWV retrieval window, performed the data validation
662 and tested most of the data application described in this paper. Amir Souri performed the WRF
663 simulations and data assimilation experiment presented in this paper. Gonzalo González Abad
664 developed and maintained the SAO retrieval code and implemented OMI TCWV data production
665 for the Aura Validation Data Center. Xiong Liu developed the OMI ozone profile retrieval and
666 provided the relevant data used in the AR application. Kelly Chance is the PI of the NASA grant,
667 and is responsible for the overall direction and execution of the project. Huiqun Wang prepared
668 and revised the manuscript with contributions from all co-authors. All authors contributed to
669 technical and scientific discussions during this project.

670

671 **Competing interests**

672 The authors declare that they have no conflict of interest.

673

674 **Acknowledgement**

675 We thank NASA's ACMAP program (Grant NNX17AH47G) for support.

676 **References**

- 677 Brion, J., Chakir, A., Daumont, D., Malicet, J. and Parisse, C.: High-resolution laboratory
678 absorption cross section of O₃ - temperature effect, *Chem. Phys. Lett.*, 213 (5-6), 610-612,
679 doi:10.1016/0009-2614(93)89169-1, 1993.
- 680 Chance, K. and Spurr, R. J. D.: Ring effect studies: Rayleigh scattering, including molecular
681 parameters for rotational Raman scattering, and the Fraunhofer spectrum, *Applied optics*,
682 36, No. 21, 5224-5230, 1997.
- 683 Chance, K., Kurosu, T. P., Sioris, C. E.: Undersampling correction for array detector-based
684 satellite spectrometers. *Appl. Opt.*, 44, 1296-1304, doi:10.1364/AO.44.001296, 2005.
- 685 Chen, F. and J. Dudhia: Coupling an Advanced Land Surface-Hydrology Model with the Penn
686 State-NCAR MM5 Modeling System. Part I: Model Implementation and Sensitivity. *Mon.*
687 *Wea. Rev.*, 129, 569-585, 2001.
- 688 Dee, D. P., Uppala, S. M., Simmons, A. J., Berrisford, P., Poli, P., et al.: The ERA-Interim
689 reanalysis: configuration and performance of the data assimilation system, *Q. J. R.*
690 *Meteorol. Soc.*, 137, 553-597, 2011.
- 691 Diedrich, H., Wittchen, F., Preusker, R., and Fischer, J.: Representativeness of total column
692 water vapour retrievals from instruments on polar orbiting satellites, *Atmos. Chem. Phys.*,
693 16, 8331-8339, doi:10.5194/acp-16-8331-2016, 2016.
- 694 Dobber, M., Voors, R., Dirksen, R., Kleipool, Q. and Levelt, P.: The high-resolution solar
695 reference spectrum between 250 and 550 nm and its application to measurements with the
696 Ozone Monitoring Instrument, *Solar Physics*, 249, 2, 281-291, doi:10.1007/s11207-008-
697 9187-7, 2008.
- 698 Ek, M. B., Mitchell, K. E., Lin, Y., Rogers, E., Grunmann, P., Koren, V., et al.: Implementation
699 of Noah land surface model advances in the National Centers for Environmental Prediction
700 operational mesoscale Eta model. *Journal of Geophysical Research:*
701 *Atmospheres*, 108(D22), 2003.
- 702 Gelaro, R., McCarty, W., Suarez, M. J., Todling, R., Molod, A., et al.: The Modern-Era
703 retrospective analysis for research and applications, Version 2 (MERRA-2), *J. Climate*, 30,
704 5419-5454, doi:10.1175/JCI-D-16-0758.1, 2017

705 Gimeno, L., Nieto, R., Vazquez, M. and Lavers, D. A.: Atmospheric rivers: a mini-review,
706 *Frontiers in Earth Sci.*, 2, Art. 2, doi:10.3389/feart.2014.00002, 2014.

707 González Abad, G., Liu, X., Chance, K., Wang, H., Kurosu, T. P. and Suleiman, R.: Updated
708 Smithsonian Astrophysical Observatory Ozone Monitoring Instrument (SAO OMI)
709 formaldehyde retrieval, *Atmos. Meas. Tech.*, 8, 19-32, doi:10.5194/amt-8-19-2015, 2015.

710 Hong, S. Y. and Lim, J. O. J.: The WRF single-moment 6-class microphysics scheme
711 (WSM6). *J. Korean Meteor. Soc.*, 42(2), 129-151, 2006.

712 Hong, S. Y., Noh, Y. and Dudhia, J.: A new vertical diffusion package with an explicit treatment
713 of entrainment processes. *Monthly weather review*, 134(9), 2318-2341, 2006.

714 Huang, G., Liu, X., Chance, K., Yang, K., Bhartia, P. K., Cai, Z., Allaart, M., Ancellet, G.,
715 Calpini, B., Coetzee, G. J. R., et al.: Validation of 10-year SAO OMI ozone profile
716 (PROFOZ) product using ozonesonde observations, *Atmos. Meas. Tech.*, 10, 7,
717 doi:10.5194/amt-10-255-2017, 2017.

718 Huang, G., Liu, X., Chance, K., Yang, K., Cai, Z.: Validation of 10-year SAO OMI ozone profile
719 (PROFOZ) product using Aura MLS measurements, *Atmos. Meas. Tech.*, 11, 1, 17-32,
720 doi:10.5194/amt-11-17-2018, 2018.

721 Kain, J.S.: The Kain–Fritsch convective parameterization: an update. *Journal of applied*
722 *meteorology*, 43(1), 170-181, 2004.

723 Kleipool, Q. L., Dobber, M. R., de Hann, J. F., and Levelt, P. F.: Earth surface reflectance
724 climatology from 3 years of OMI data, *J. Geophys. Res.*, 113, D18308,
725 doi:10.1029/2008JD010290, 2008.

726 Lampel, J., Frieß, and Platt, U.: The impact of vibrational Raman scattering of air on DOAS
727 measurements of atmospheric trace gases, *Atmos. Meas. Tech.*, 8, 3767-3787,
728 doi:10.5194/amt-8-3767-2015, 2015a.

729 [Lampel, J., Pohler, D., Tschirter, J., Friess, U., Platt, U.: On the relative absorption strengths of](#)
730 [water vapour in the blue wavelength range, *Atmos. Meas. Tech.*, 8, 4329-4346,](#)
731 [doi:10.5194/amt-8-4329-2015, 2015b.](#)

732 Liu, X., Bhartia, P. K., Chance, K., Spurr, R. J. D., Kurosu, T. P.: Ozone profile retrievals from
733 the Ozone Monitoring Instrument, *Atmos. Chem. Phys.*, 10, 2521-2537, doi:10.5194/acp-
734 10-2521-2010, 2010.

735 Lorente, A., Boersma, K. F., Yu, H., Dorner, S., Hillboll, A., Richter, A., Liu, M., Lamsal, L. N.,
736 Barkley, M., De Smedt, I., Van Roozendaal, M., Wang, Y., Wagner, T., Beirle, S., Lin, J.,
737 Krotkov, N., Stammes, P., Wang, P., Eskes, H. J. and Krol, M.: Structural uncertainty in air
738 mass factor calculation for NO₂ and HCHO satellite retrievals, *Atmos. Meas. Tech.*, 10,
739 759-782, doi:10.5194/amt-10-759-2017, 2017.

740 Levelt, P. F., van den Oord, G. H., Dobber, M. R., Malkki, A., Visser, H., de Vries, J., Stammes,
741 P., Lundell, J. O. and Saari, H.: The ozone monitoring instrument, *T. Geosci. Remote*, 44,
742 1093-1101, 2006.

743 Mason, J. D., Cone, M. T. and Fry, E. S.: Ultraviolet (250-550 nm) absorption spectrum of pure
744 water, *Applied optics*, 55, No. 25, 7163-7172, doi:10.1364/AO.55.007163, 2016

745 Mears, C. A., Wang, J., Smith, D. and Wentz, F. J.: Intercomparison of total precipitable water
746 measurements made by satellite-borne microwave radiometers and ground-based GPS
747 instruments, *J. Geophys. Res. Atmos.*, 120, 2492-2504, doi:10.1002/2014JD022694, 2015.

748 Neiman, P. J., Ralph, F. M., Wick, G. A., Kuo, Y., Wee, T., Ma, Z., Taylor, G. H., Dettinger, M.
749 D.: Diagnosis of an intense atmospheric river impacting the Pacific northwest: storm
750 summary and offshore vertical structure observed with COSMIC satellite retrievals,
751 *Monthly Wea. Rev.*, 136, 4398 – 4420, doi:10.1175/2008MWR2550.1, 2008a.

752 [Neiman, P. J., Ralph, F. M., Wick, G. A., Lundquist, J. D., Dettinger, M. D.: Meteorological](#)
753 [characteristics and overland precipitation impacts of atmospheric rivers affecting the West](#)
754 [Coast of North America based on eight years of SSM/I satellite observations, *J.*](#)
755 [Hydrometeorology](#), 9, 22-47, doi:10.1175/2007JHM855.1, 2008b.

756 Ning, T., Wang, J., Elgered, G., Dick, G., Wickert, J., Bradke, M., Sommer, M., Querel, R. and
757 Smale, D.: The uncertainty of the atmospheric integrated water vapour estimated from
758 GNSS observations, *Atmos. Meas. Tech.*, 9, 79-92, doi:10.5194/amt-9-79-2016, 2016.

759 Noël, S., Buchwitz, M., Bovensmann, H., Hoogen, R., and Burrows, J. P.: Atmospheric Water
760 Vapor Amounts Retrieved from GOME Satellite data, *Geophys. Res. Lett.*, 26, 1841–1844,
761 1999.

762 Rodgers, C. D.: Inverse methods for atmospheric sounding, theory and practice, Series on
763 Atmospheric, Ocean and Planetary Physics – Vol. 2, Editor: Taylor, F. W., Published by
764 World Scientific Publishing Co. Pte. Ltd., Singapore, 2000.

765 [Schröder, M., Lockhoff, M., Shi, L., August, T., Bennartz, R., et al.: The GEWEX Water Vapor](#)
766 [Assessment: Overview and introduction to results and recommendations, *Remote Sensing*,](#)
767 [11, 3, doi:10.3390/rs11030251, 2019.](#)

768 Skamarock W. C. and Klemp, J. B.: A time-split nonhydrostatic atmospheric model for weather
769 research and forecasting applications, *J. Computational Physics*, 227, 2, 3465-3485,
770 doi:10.1016/j.jcp.2007.01.037, 2008.

771 Palmer, P. I., Jacob, D. J., Chance, K., Martin, R. V., Spurr, R. J. D., Kurosu, T. P., Bey, I.,
772 Rantosca, R., Fiore, A. and Li, Q.: Air mass factor formulation for spectroscopic
773 measurements from satellites: Application to formaldehyde retrievals from the Global
774 Ozone Monitoring Experiment, *J. Geophys. Res.*, 106, D13, 14539-14550, 2001.

775 Ralph, F. M., Neiman, P. J. and Wick, G. A.: Satellite and CALJET aircraft observations of
776 atmospheric rivers over the eastern north Pacific ocean during the winter of 1997/98,
777 *Monthly Wea. Rev.*, 132, 1721-1745, doi:10.1175/1520-
778 0493(2004)132<1721:SACAOO>2.0.CO;2, 2004.

779 Rothman, L. S., Gordon, I. E., Barbe, A., Benner, D. C., Bernath, P. F., et al.: The HITAN 2008
780 molecular spectroscopic database, *J. Quant. Spectr. Radiat. Tran.*, 110, 533-572, 2009.

781 Schmidt, G. A., Ruedy, R. A., Miller, R. L. and Lacis, A. A.: Attribution of the present-day total
782 greenhouse effect, *J. Geophys. Res.*, 115, D20106, doi:10.1029/2010JD014287, 2010.

783 Schroder, M., Lockhoff, M., Fell, F., Forsythe, J., Trent, T., Bennartz, R., Borbas, E., Bosilovich,
784 M. G., Castelli, E., Hersbach, H., Kachi, M., Kobayashi, S., Kursinski, E. R., Loyola, D.,
785 Mears, C., Preusker, R., Rossow, W. B. and Saha, S.: The GEWEX water vapor assessment
786 archive of water vapour products from satellite observations and reanalyses, *Earth Syst.*
787 *Sci. Data*, 10, 1093-1117, doi:10.5194/essd-10-1093-2018, 2018.

788 Shi, L., Schreck, C. J. III, and Schroder, M.: Assessing the pattern differences between satellite-
789 observed upper tropospheric humidity and total column water vapor during major El Niño
790 events, *Remote Sens.*, 10, 1188, doi:10.3390/rs10081188, 2018.

791 Spietz, P., Martin, J. C. G. and Burrows, J. P.: Spectroscopic studies of the I-2/O-3
792 photochemistry – Part 2. Improved spectra of iodine oxides and analysis of the IO
793 absorption spectrum, *J. Photochemistry and Photobiology*, 176 (1-3), 50-67,
794 doi:10.1016/j.photochem.2005.08.023, 2005.

795 Thalman, R. and Volkamer, R.: Temperature dependent absorption cross-sections of O₂-O₂
796 collision pairs between 340 and 630 nm and at atmospherically relevant pressure, *Phys.*
797 *Chem. Chem. Phys.*, 15, 15371-15381, doi:10.1039/c3cp50968k, 2013.

798 Vandaele, A. C., Hermas, C., Simon, P. C., Carleer, M., Colin, R., Fally, S., Merienne, M. F.,
799 Jenouvier, A. and Coquart, B.: Measurements of the NO₂ absorption cross-section from
800 42000 cm⁻¹ to 10000 cm⁻¹ (238-1000 nm) at 200 K and 294 K, *J. Quant. Spectr.*
801 *Radiat. Trans.*, 59, 171-184, doi:10.1016/S0022-4073(97)00168-4, 1998.

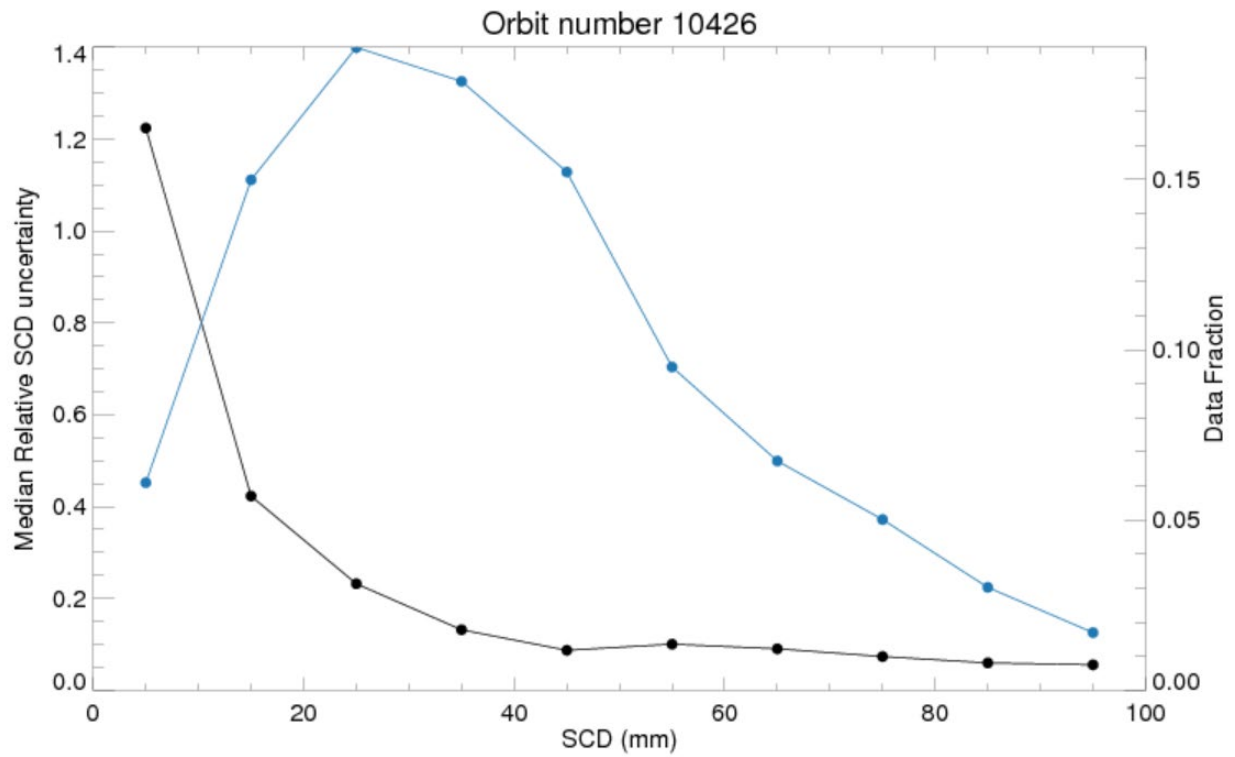
802 Vasilkov, A., Qin, W., Krotkov, N., Lamsal, L., Spurr, R., Haffner, D., Joiner, J., Yang, E. and
803 Marchenko, S.: Accounting for the effects of surface BRDF on satellite cloud and trace-gas
804 retrievals: a new approach based on geometry-dependent Lambertian equivalent reflectivity
805 applied to OMI algorithms, *Atmos. Meas. Tech.*, 10, 333-349, doi:10.5194/amt-10-333-
806 2017, 2017.

807 Veefkind, J. P., de Hann, J. F., Sneep, M. and Levelt, P. F.: Improvements to the OMI O₂-O₂
808 operational cloud algorithm and comparisons with ground-based radar-lidar observations,
809 *Atmos. Meas. Tech.*, 9, 6035-6049, doi:10.5194/amt-9-6035-2016, 2016.

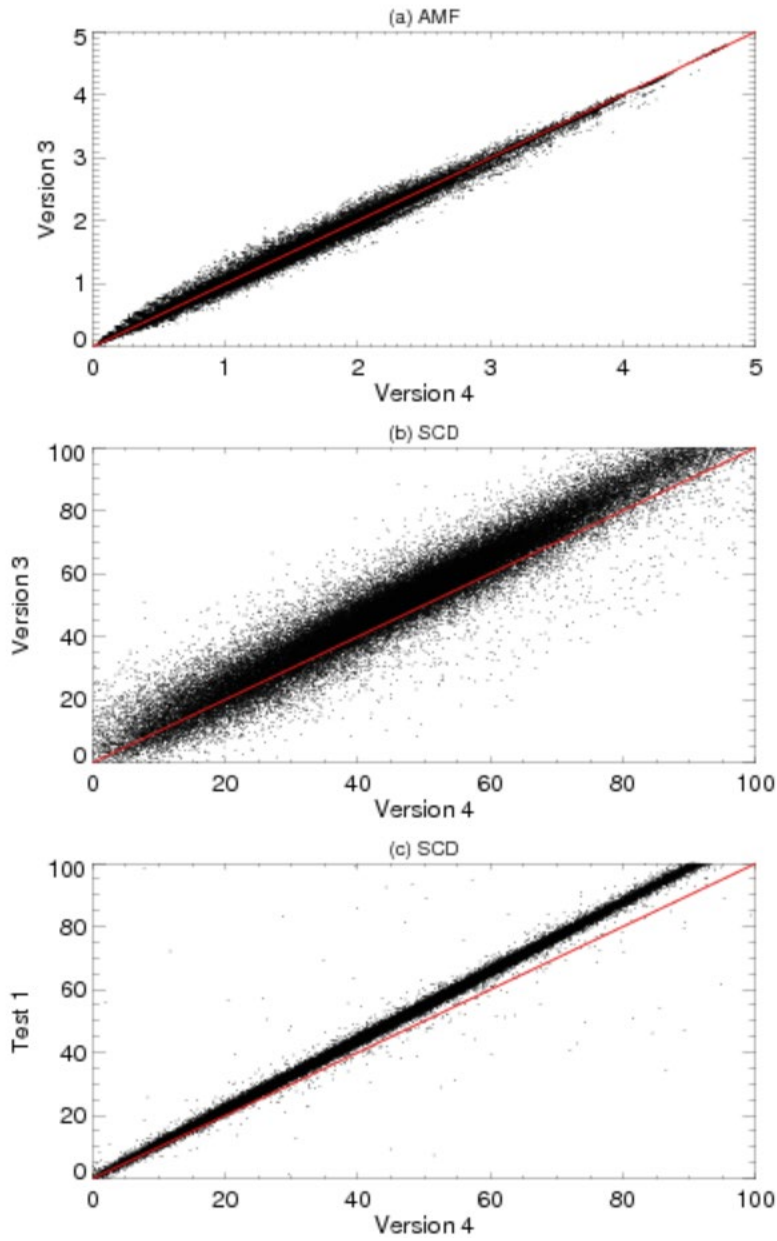
810 Volkamer, R., Spietz, P., Burrows, J. and Platt, U.: High-resolution absorption cross section of
811 glyoxal in the UV/Vis and IR spectral ranges, *J. Photochem. Photobio.*, 172, 35-46,
812 doi:10.1016/j.jphotochem.2004.11.011, 2005.

813 Wagner, T., Beirle, S., Sihler, H. and Mies, K.: A feasibility study for the retrieval of the total
814 column precipitable water vapour from satellite observations in the blue spectral range,
815 *Atmos. Meas. Tech.*, 6, 2593-2605, doi:10.5194/amt-6-2593-2013, 2013.

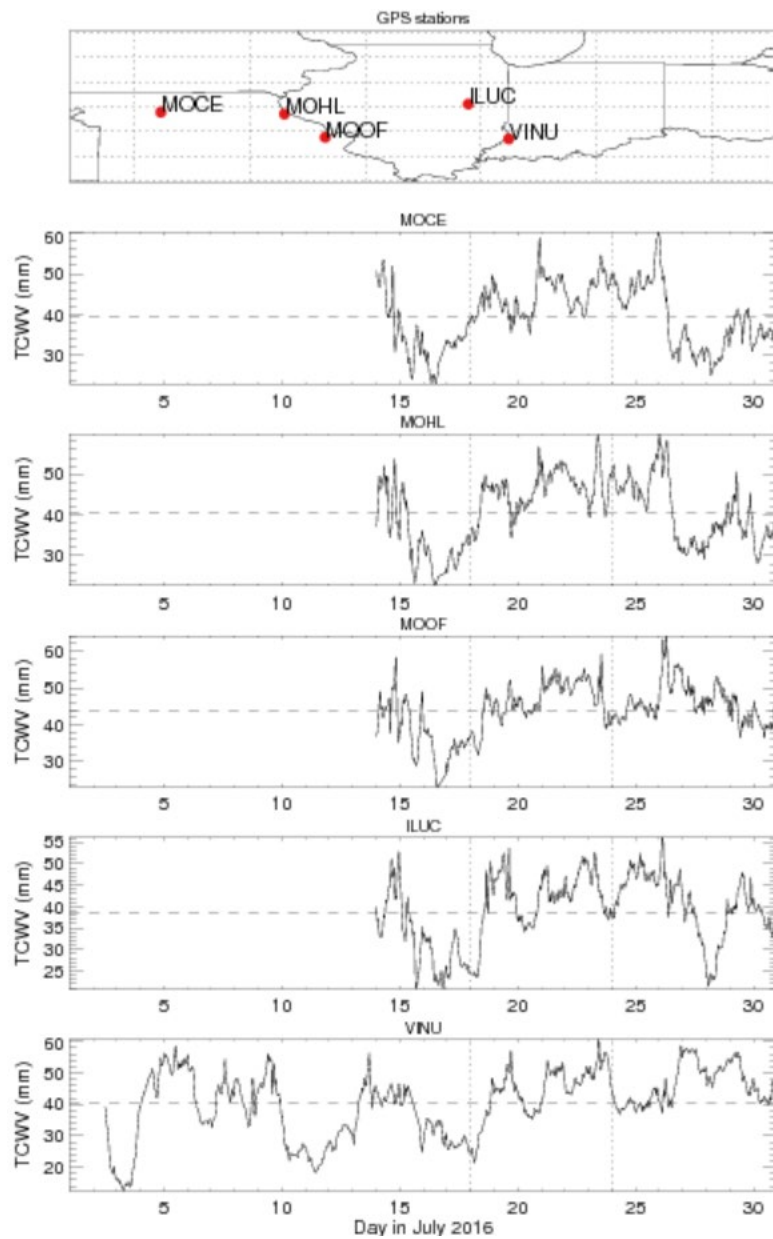
- 816 Wang, H., Liu, X., Chance, K., González Abad, G. and Chan Miller, C.: Water vapor retrieval
817 from OMI visible spectra, *Atmos. Meas. Tech.*, 7, 1901-1913, doi:10.5194/amt-7-1901-
818 2014, 2014.
- 819 Wang, H., González Abad, G., Liu, X. and Chance, K.: Validation and update of OMI total
820 column water vapor product, *Atmos. Chem. Phys.*, 16, 11379-11393, doi:10.5194/acp-16-
821 11379-2016, 2016.
- 822 Wentz, F. J.: A well-calibrated ocean algorithm for special sensor microwave/imager, *J.*
823 *Geophys. Res.*, 102(C4), 8703-8718, doi:10.1029/96JC01751, 1997.
- 824 Wolter, K. and Timlin, M.S.: Measuring the strength of ENSO events - how does 1997/98 rank?
825 *Weather*, 53, 315-324, 1998.
- 826 Zhu, Y. and Newell, R. E.: A proposed algorithm for moisture fluxes from atmospheric rivers,
827 *Monthly Weather Rev.*, 126, 3, 725-735, doi:10.1175/1520-
828 0493(1998)126<0725:APAFMF>2.0.CO;2, 1998.



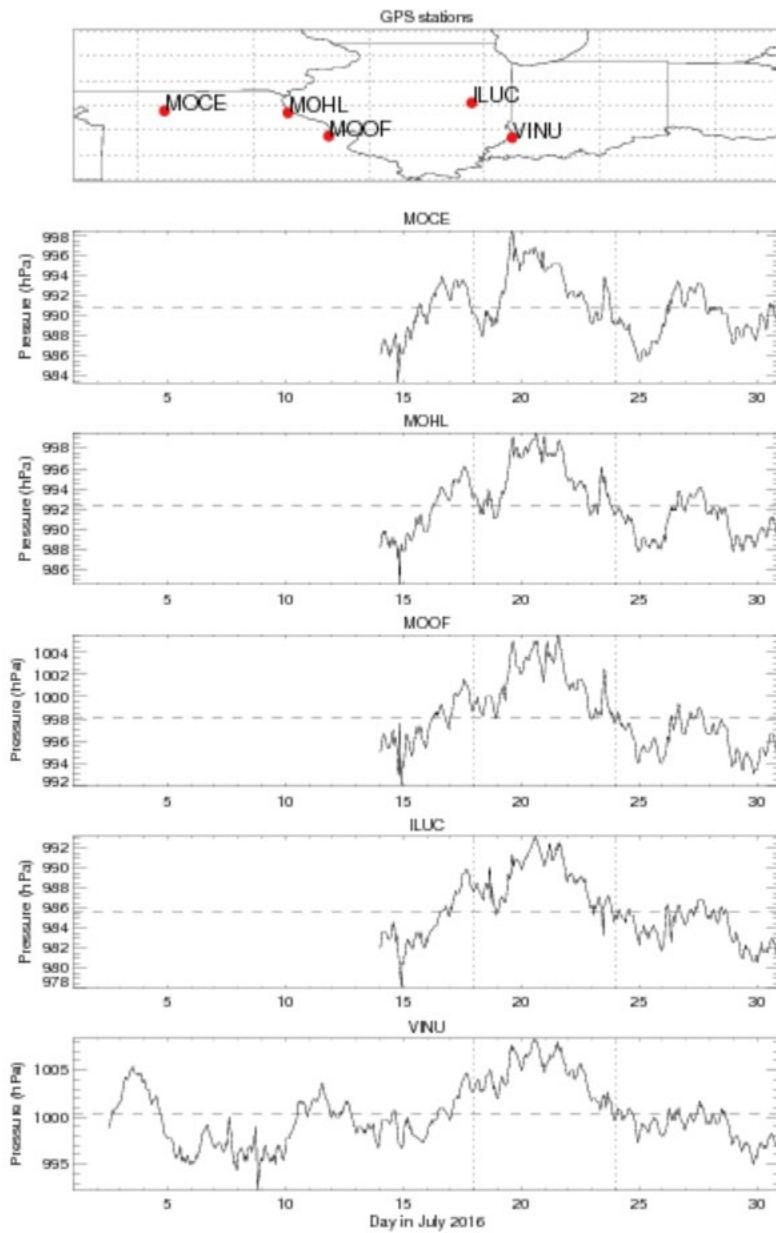
Supplementary Figure 1. Black curve shows the median relative SCD uncertainty for each 10 mm SCD bin (left axis). Blue curve shows the fraction of data points that fall within each 10 mm SCD bin (right axis). Results are derived from OMI orbit number 10426.



Supplementary Figure 2. (a) Version 4.0 versus Version 3.0 AMF comparison; (b) Version 4.0 versus Version 3.0 SCD comparison; (c) Version 4.0 versus Test 1 SCD comparison. Test 1 has the same setting as Version 4.0 except that water vapor reference spectrum is from HITRAN 2016. All results are for OMI orbit number 10423.



Supplementary Figure 3. Time series of TCWV (mm) observed by each GPS station indicated in the top panel for July 2016. The horizontal dashed lines indicate the mean TCWV for July. The two dotted vertical lines bracket the corn sweat time period discussed in the paper.



Supplementary Figure 4. Time series of surface pressure (hPa) observed by each GPS station indicated in the top panel for July 2016. The horizontal dashed lines indicate the mean surface pressure for July. The two dotted vertical lines bracket the corn sweat time period discussed in the paper.